A half-centre oscillator encodes sleep pressure

Peter S. Hasenhuetl[1,2], Raffaele Sarnataro[1,2], Eleftheria Vrontou[1], H. Olof Rorsman[1], Clifford B. Talbot[1], Ruth Brain[1], and Gero Miesenböck[1,*]

[1] Centre for Neural Circuits and Behaviour, University of Oxford, Tinsley Building, Mansfield Road, Oxford, OX1 3SR, UK.

[2] These authors contributed equally: P.S.H and R.S.

* Correspondence: gero.miesenboeck@cncb.ox.ac.uk

Summary

Oscillatory neural dynamics are an inseparable part of mammalian sleep. Characteristic rhythms are associated with different sleep stages and variable levels of sleep pressure, but it remains unclear whether these oscillations are passive mirrors or active generators of sleep. Here we report that sleep-control neurons innervating the dorsal fan-shaped body of *Drosophila* (dFBNs) produce slow-wave activity (SWA) in the delta frequency band (0.2–1 Hz) that is causally linked to sleep. The dFBN ensemble contains one or two rhythmic cells per hemisphere whose membrane voltages oscillate in anti-phase between hyperpolarized DOWN and depolarized UP states releasing bursts of action potentials. The oscillations rely on direct interhemispheric competition of two inhibitory half-centres connected by glutamatergic synapses. Interference with glutamate release from these synapses disrupts SWA and baseline as well as rebound sleep, while the optogenetic replay of SWA (with the help of an intersectional, dFBN-restricted driver) induces sleep. Rhythmic dFBNs generate SWA throughout the sleep–wake cycle—despite a mutually antagonistic 'flip-flop' arrangement with arousing dopaminergic neurons—but adjust its power to sleep need via an interplay of sleep history-dependent increases in dFBN excitability and homeostatic depression of their efferent synapses, as we demonstrate transcriptionally, structurally, functionally, and with a simple computational model. The oscillatory format permits a durable encoding of sleep pressure over long time scales but requires downstream mechanisms that convert the amplitude-modulated periodic signal into binary sleep–wake states.

Introduction

The dynamics of neurons responsible for the homeostatic regulation of sleep, like those of all feedback controllers, are coupled to the dynamics of the controlled object: the outputs of one system serve as inputs to the other. Studies in *Drosophila* have begun to paint a detailed picture of how sleep-inducing neurons sense changes in the physiology of the sleeping and waking organism. Sleep-control neurons[1,2] with projections to the dorsal layers of the fan-shaped body (dFBNs) estimate sleep pressure by monitoring the flow of electrons through their own mitochondria[3]. Sleep loss creates an imbalance between electron supply and ATP demand[4] that diverts high-energy electrons from the respiratory chain into uncontrolled side reactions with molecular O_2, producing reactive oxygen species[3] which fragment the polyunsaturated fatty acyl (PUFA) chains of membrane lipids into short- or medium-chain carbonyls[5]. dFBNs count the release of PUFA-derived carbonyls (and transduce this signal into sleep) in a process that involves an allosteric dialogue between the voltage-gated potassium channel Shaker—a critical determinant of dFBN activity[6]—and its redox-sensitive β-subunit Hyperkinetic[3,5].

These insights were gained in experiments which clamped certain variables in order to isolate others. For example, to determine how sleep history[2] or mitochondrial dynamics[4] alter the current–spike frequency function of dFBNs, the neurons were driven with fixed current patterns; to resolve how cellular redox chemistry[3], lipid peroxidation products[5], or arousing dopamine[6] modulate particular ion channels, the membrane potential of dFBNs was stepped between fixed voltages. How the unclamped dFBN population responds to changes in sleep pressure, and how these responses alter the sleep–wake state of the organism, therefore remains unknown.

Results

dFBN slow oscillations

To visualize unperturbed dFBN ensemble activity *in vivo*, we expressed the genetically encoded Ca^{2+}-sensor GCaMP6f (GCaMP in brief) under the control of *R23E10-GAL4* and imaged the dendritic tufts of dFBNs by two-photon microscopy. Dendritic fluorescence displayed prominent Ca^{2+} transients, which were often visible by naked eye and repeated rhythmically at 0.2–1 Hz (Fig. 1a). Following the convention in mammals[7], we refer to activity in the frequency band of 0.2–2 Hz as delta or slow-wave activity (SWA).

The regularity of GCaMP transients across the dataset in Fig. 1a raises the question of whether the entire dFBN population is engaged in synchronous oscillations, or whether only a subset of pacemaker cells dominates dendritic fluorescence, which represents a weighted sum of contributions from all dFBN processes in the imaged region. To distinguish these possibilities, we recorded simultaneous GCaMP signals from a median of 8 cell bodies (range: 3–12) in the same hemisphere (Fig. 1b). The time courses of somatic Ca^{2+} changes varied widely among members of the dFBN ensemble and in most neurons showed no discernible temporal structure or sign of cell-to-cell coordination (Pearson $r = 0.05 \pm 0.15$, mean ± s.d). The notable exceptions were one or two rhythmic neurons per hemisphere, which produced continuous, pacemaker-like Ca^{2+} oscillations in the delta band or slow (on time scales of tens of s) modulations of intermittent periods of delta activity (Fig. 1b, c). The prominent rhythm of these neurons drowned out the majority of cells in highly correlated dendritic and axonal ensemble signals (Supplementary Fig. 1a–c). An important proviso of our study is therefore that it speaks only for this minority of dFBNs.

To characterize the electrical events underlying GCaMP transients in rhythmic dFBNs, we performed simultaneous whole-cell patch-clamp and two-photon Ca^{2+}-imaging experiments *in vivo*. The superimposition of voltage and GCaMP traces in Fig. 1d shows that Ca^{2+} transients coincided with large, sustained depolarizations generating high-frequency action potential bursts. These UP states alternated with DOWN states of somewhat longer average duration during which the neurons were hyperpolarized and stopped firing. For a quantitative analysis, we estimated the GCaMP impulse response function from these recordings and used it successfully to predict fluorescence signals from the action potential record (Fig. 1d, e). A spike frequency histogram aligned to the onset of GCaMP transients peaked ~120 ms before the maximal fluorescence change (Fig. 1f).

A half-centre oscillator generates SWA

Rhythmic neural activity is typically a product of cell-intrinsic oscillators, such as hyperpolarization-activated cation channels[8], or oscillatory circuits, which abound in the neural control of movement[9-12] but have also been proposed to regulate sleep cycle time[13,14], if not sleep itself. In a prototypical oscillatory circuit, exemplified by the two-neuron swimming system of *Clione*[10] or the myriad central pattern generators that populate invertebrate ganglia or the vertebrate brain stem, mutual inhibition between two half-centres controlling opponent sets of muscles produces self-perpetuating cyclic movement[9-12]. In the minimal swim circuit of *Clione*, reciprocal inhibition is in fact the only synaptic interaction between the two component neurons[10].

Analyses of dFBN activity, along with connectomic evidence[15], indicate that two mutually inhibitory half-centres are responsible for the generation of SWA. Simultaneous bilateral recordings showed that Ca^{2+} transients in dFBNs of the left and right hemispheres alternated out of phase (Fig. 2a), so that the occurrence of a fluorescence maximum in one hemisphere was associated, on average, with a minimum in the other (Fig. 2b, c). In keeping with the idea that direct inhibition from the contralateral hemisphere is the source of the negative fluorescence deflection, the GCaMP signal dipped deeper the higher was the mean SWA power in both hemispheres (Fig. 2d). As expected for two neuronal populations synchronized in antiphase, interhemispheric cross-correlations returned minima at a lag of 0 s and a period of ~2 s, corresponding to 0.5 Hz (Fig. 2e).

The symmetry and strength of connections among dFBNs in the *Drosophila* hemibrain connectome[15] meets the anatomical requirements of a half-centre oscillator. An almost perfectly symmetric weighted connectivity matrix, exhibiting a correlation coefficient of 0.92 with its transpose and a weight distribution indistinguishable from an undirected graph (Supplementary Fig. 2a), links the members of the population. Although dFBN interconnectivity is generally dense (full dFBN network: 0.73; dFBNs within layer 6: 0.96; dFBNs within layer 7: 0.96), there are two stand-outs in a heavy-tailed distribution of connection weights: two layer 6-projecting dFBN types[15] (one member of the FB6A class and the single neuron FB6E) form exceptionally numerous, exclusively interhemispheric, reciprocal synapses with their contralateral counterparts (Supplementary Fig. 2b, c). We note that one or two neurons per hemisphere display robust SWA (Fig. 1c) and tentatively equate these cells with FB6A and FB6E.

Single-cell transcriptomic data reported in a companion paper[4] identify glutamate as the fast-acting transmitter of dFBNs, in agreement with existing electrophysiological evidence that transmission

from dFBNs (like glutamate release at many central synapses of *Drosophila*[16]) is inhibitory[17]. We confirmed this transmitter assignment anatomically and functionally. The subtraction of glutamatergic neurons from the *R23E10-GAL4* pattern (*R23E10-GAL4* \ *VGlut-GAL80*) retained two pairs of GABAergic cells in the suboesophageal zone and a handful of cholinergic neurons in the ventral nerve cord but excluded all dFBNs (Fig. 3a, b, Supplementary Fig. 3a, Supplementary Video 1); conversely, the intersection of the *R23E10-GAL4* pattern with glutamatergic neurons (*R23E10* ∩ *VGlut-GAL4*, created by reconstituting GAL4 from hemidrivers *R23E10-DBD* and *VGlut-p65AD*) consisted exclusively of dFBNs (Fig. 3c, Supplementary Fig. 3b, Supplementary Video 2). dFBNs coexpressing the optogenetic actuator CsChrimson and the glutamate sensor iGluSnFR responded to light pulses with stimulus-locked fluorescence transients in their axonal fields, verifying synaptic glutamate release (Fig. 3d). For a demonstration that dFBNs themselves are targets of dFBN-mediated inhibition, we divided the dFBN ensemble randomly, via stochastic recombination of GAL4-responsive FLP-out constructs[18], into two disjoint groups containing either a green fluorophore (GCaMP for imaging; alternatively mCD8::GFP for targeted whole-cell electrophysiology) or CsChrimson::tdTomato (Supplementary Fig. 3c). Optical stimulation of the CsChrimson-expressing set resulted in reductions of GCaMP fluorescence in the complementary set of dFBNs in imaging experiments (Fig. 3e), or in hyperpolarization and the suppression of spiking in current-clamp recordings from GFP-positive (and therefore CsChrimson-negative) neurons (Fig. 3f). The addition of tetrodotoxin eliminated action potentials but not inhibitory postsynaptic potentials (Fig. 3f), which persist when transmission from directly connected terminals is triggered by light[18]. dFBN-to-dFBN communication is therefore monosynaptic.

The dense inhibitory interconnectivity of dFBNs (Fig. 3e, f, Supplementary Fig. 2) complicates attempts to control their activity, and the practice and interpretation of stimulation experiments therefore requires some thought. Hard, unrelenting, bilateral depolarization of dFBNs establishes a tug of war between the externally imposed excitation and the powerful all-to-all inhibition it elicits, with sometimes unexpected consequences. Failures to observe increases in sleep[19,20] (or even seemingly paradoxical sleep losses[21]) after presumed activation of dFBNs led to claims that the neurons are ineffective in promoting sleep[20], when it was in fact the stimulation protocols that proved ineffective: pulsed illumination, which avoids a lasting cross-inhibitory stalemate, readily induced sleep in flies expressing CsChrimson under the control of *R23E10* ∩ *VGlut-GAL4* exclusively in dFBNs (Fig. 3g), even though neurons of both hemispheres were inevitably driven in synchrony rather than their natural antiphase. As in the regulation of sleep quality by clock neurons[22] and the control of cortical SWA by the midline thalamus[23], the temporal structure of the optical

stimulus train mattered: increases in sleep quantity followed the simulated convergence of alternating 500-ms action potential bursts from the left and right hemispheres in the axonal target layer of dFBNs (which we recreated by compressing 10 light pulses into one half of a 500:500 ms duty cycle; Fig. 3g) but were absent when the same number of pulses were spread evenly across time, mimicking tonic 10-Hz activity (Fig. 3g).

To add evidence of necessity to this demonstration of sufficiency, we selectively incapacitated dFBNs by RNA-mediated interference (RNAi) with the expression of VGlut in the entire *R23E10-GAL4* domain, of which dFBNs are the sole glutamatergic members (Fig. 3b, c). The expression of four out of four independent *VGlut*^{RNAi} transgenes led to the expected reductions in sleep (Fig. 3h), in most cases without any potentially confounding waking hyperactivity (Supplementary Fig. 3d). Consistent with a critical role of reciprocal inhibition in the generation of antiphase oscillations[9-12], and of dFBN output in sleep homeostasis[2], interference with glutamatergic transmission also disrupted SWA (Fig. 3i, Supplementary Fig. 3e) and the homeostatic response to sleep loss (Fig. 3j).

SWA encodes sleep pressure

The sleep deficits following the dissolution of SWA hint, and the sleep gains due to SWA replay over tonic stimulation strongly suggest, that slow waves have an instructive role in the translation of sleep pressure into sleep (Fig. 3g–j). The electroencephalogram (EEG) during mammalian non-rapid eye movement (NREM) sleep[7,24] is characterized by SWA that reflects synchronous transitions of cortical neurons between depolarized UP and hyperpolarized DOWN states[25], not unlike those of rhythmic dFBNs (Fig. 1d). Cortical SWA is a classical EEG marker of sleep pressure: SWA levels at sleep onset increase after prolonged wakefulness and decrease after sleep[26]. To search for analogous modulations of dFBN activity, we compared SWA in flies that had been mechanically sleep-deprived during the preceding night with rested controls. Sleep deprivation increased the average peak amplitude of GCaMP transients (Fig. 4a, b) and the mean power in the delta range but left other frequency bands unchanged (Fig. 4c). As flies recovered, SWA power decayed back to baseline over the course of 12–24 hours (Fig. 4d). Following an unperturbed night of rest, in contrast, SWA was at its minimum in the morning (zeitgeber time 0), rose naturally during the day to an evening peak (zeitgeber time 12), and declined again during sleep (Fig. 4d).

Previous reports of sleep-related rhythms[27,28], and in particular observations of SWA in parts of the central complex[29,30] (R5 neurons and dFBNs), noted but could not explore possible parallels with NREM sleep because the studies were performed *ex vivo* and without a simultaneous behavioral

read-out of vigilance state. It is thus unclear if the occurrence of dFBN delta oscillations defines a slow-wave sleep stage as in mammals or if SWA tracks variations in sleep pressure throughout the sleep–wake cycle. To resolve this point, we examined if dFBN oscillations persisted during a behaviorally verified state of arousal. Head-fixed flies expressing either the dopamine sensor $GRAB_{DA2m}$ or GCaMP in dFBNs were placed on a spherical treadmill and roused with a pulse of infrared laser light focused on their abdomina (Fig. 5a). Consistent with the notion that dopaminergic projections to the fan-shaped body mediate arousal by inhibiting dFBNs[6,31,32], activating the laser for 2 s elicited a movement bout along with dopamine release onto the neurons' dendrites (but not axons) (Fig. 5b). Like spontaneous spiking during dendritic applications of exogenous dopamine or optogenetic stimulation of dopaminergic neurons[6], Ca^{2+} oscillations collapsed briefly during a short heat stimulus but resumed thereafter, following a powerful postinhibitory rebound (Fig. 5c–e), while pharmacological doses of dopamine[6] produced pauses lasting many seconds (Supplementary Fig. 4).

Coincident optogenetic activation of dFBNs reduced the amplitude of heat-evoked dopamine transients (Fig. 5f, g), indicating that dFBNs and dopaminergic neurons antagonize each other in an arrangement reminiscent of the inhibitory flip-flop between sleep- and wake-promoting neurons in the mammalian hypothalamus[33].

Glutamate release adjusts to sleep pressure

In contrast to SWA in mammals, which can be recorded across the entire cortical surface during NREM sleep[7], dFBN slow waves are products of an anatomically circumscribed central pattern generator that may be numerically as simple as the two-neuron swim circuit of *Clione*[10]. Despite their apparent simplicity, central pattern generators are notorious for the sensitivity of their dynamics to modulatory changes in biophysical parameters[34-36]. dFBNs experience many such changes as sleep pressure builds: they steepen their current–spike frequency functions[2,3], modulate voltage-gated and leak potassium conductances in opposite directions[6], and receive heightened (indirect) excitatory drive from R5 neurons[37]. Single-cell transcriptomic data reported in a companion study[4] suggest that these changes, which all enhance activity, are counterbalanced by a weakening of dFBN efferent synapses. Sleep deprivation was found selectively to downregulate gene products with roles in synapse assembly, active zone maintenance, synaptic vesicle release, and presynaptic homeostatic plasticity[4,38]. Prominent among these differentially expressed genes was *bruchpilot* (*brp*), which encodes a core structural component of active zones[39,40]. Tagging the endogenous BRP protein with a V5 peptide through dFBN-restricted genomic recombination[41] allowed us to quantify its abundance as a function of sleep history. In a clear reflection of the transcriptional picture[4], the intensity of

BRP::V5 fluorescence (normalized to that of mCD8::GFP), an index of active zone size and a structural correlate of synaptic strength[42], decreased at dFBN synapses of sleep-deprived flies (Fig. 6a). This is an unusual adjustment: waking experience, whether enforced by mechanical agitation or enriched by social interaction, is widely thought to lead to synaptic potentiation[43], and axon terminal numbers or BRP levels indeed increase in many parts of the sleep-deprived *Drosophila* brain[44,45], including virtually all specific neuron types that have been examined, such as R5 neurons[37] (Supplementary Fig. 5a), Kenyon cells[46], and clock neurons[44]. The anti-cyclical depression of dFBN synapses after sleep loss thus underlines, like their anti-cyclical energy metabolism does[4], their special status with respect to sleep.

For a functional confirmation under activity-normalized conditions that sleep deprivation attenuated synaptic transmission from dFBNs, we measured the optically evoked axonal release of glutamate from dFBNs co-expressing CsChrimson and iGluSnFR. Saturation hyperbolas described the dependence of transmitter secretion on light intensity irrespective of sleep history, but the iGluSnFR signal saturated at lower levels in sleep-deprived than in rested flies (Fig. 6b). The significance of presynaptic depression, which we have now demonstrated at the transcriptional[4], structural, and functional levels, for the sleep need-dependent modulation of SWA becomes clear in a simple model where two dFBNs are embedded in recurrent circuitry[17,37] and connected across the midline (Fig. 6c, Supplementary Fig. 6b). These direct, symmetric, and inhibitory connections are necessary (and must be sufficiently strong) to produce rhythmic, pacemaker-like SWA. Empirically, individual dFBNs become more excitable as sleep pressure rises[2]; artificially enhancing this excitability promotes sleep[3,4,6]; SWA power grows with sleep drive (Fig. 4c); and optogenetic replay of SWA induces sleep (Fig. 3g). However, the network's recurrent organization allows an increase in SWA following changes in intrinsic dFBN excitability and external excitatory drive only if a homeostatic weakening of dFBN synapses is part of the simulations (Fig. 6d); without it, dFBNs would cut off their own sources of excitation (Supplementary Fig. 5c). The two seemingly opposing forces observed in dFBNs after sleep deprivation—increased excitability and decreased synaptic output—may in reality work together to generate an oscillatory representation of sleep need.

Discussion

Our work, along with previous studies[27-30], has uncovered remarkable parallels and striking differences in the sleep-related neuronal dynamics of flies and mammals. Slow waves reflecting alternating UP and DOWN states are a common marker of sleep pressure, but the biophysical origin, spatial spread, and temporal persistence of these waves differ. A central pattern generator formed by as few as two dFBNs encodes sleep need in the amplitude of its periodic output, which oscillates robustly also in awake flies. It is this stability—and the considerable lengths dFBNs go to to maintain it at variable levels of sleep pressure—that poses the most intriguing questions.

What are the implications of persistent SWA for the accumulation and discharge of sleep pressure? An accompanying manuscript[5] shows that dFBNs keep a record of sleep need in a biochemical memory where each unit of storage is a Shaker–Hyperkinetic channel whose cofactor oxidation state holds one bit of information. Productive encounters with PUFA-derived carbonyls increase, whereas depolarization-controlled exchange reactions decrease, the fraction of channels with oxidized cofactors. The fill level of the integrator thus depends on a dynamic equilibrium between oxidation and exchange. Regular spikes would tip this equilibrium toward exchange and thereby introduce a leak into the integrator, extending its time constant. We currently do not know how rapidly the Hyperkinetic pool reaches capacity, but the addition of a spike-triggered leak offers flexibility to adjust the time to saturation. With a range of spiking patterns in the dFBN population, the same mechanism could in principle produce a spectrum of integration times and the characteristic heavy-tailed distribution of sleep bout durations.

dFBNs have a demonstrated ability to switch reversibly between long-lasting electrically active ON and quiescent OFF states[6]. These binary states (discovered under conditions where transmembrane currents were clamped) bracket the extremes of the dynamic range used by dFBNs to map largely cell-autonomous, sleep history-dependent metabolic variables, such as mitochondrial electron usage[3,4] or levels of peroxidized lipids[5], onto electrical signals that can be communicated to other cells. Under unclamped conditions, we now understand, this dynamic range is set so that an oscillatory representation of sleep pressure continuously flows to downstream structures, including during wakefulness. Only manipulations which forcibly block the discharge of sleep pressure appear to interrupt this periodic signal—at a price that is debited biochemically[3-5] and repaid in heightened SWA power when inhibition is released. dFBNs fall silent during applications of exogenous dopamine[6] and reduce their activity far below baseline during mechanical sleep deprivation[47];

conversely, artificial depolarization of dFBNs during enforced waking prevents the mitochondrial rearrangements that are a visible token of the associated metabolic cost[4].

The utility of communicating an unbroken record of sleep pressure to the action-selection circuitry of the fan-shaped body[15] is obvious: the likely need for future sleep is an important factor in choosing what to do now. However, if the same periodic signal also controls transitions between sleep–wake states, as our replay and interference experiments confirm, continuous variations in SWA power must be transformed into binary outcomes. This analog-to-digital conversion could take several forms. For example, dFBNs could target a dedicated sleep module[15] in the central complex through strongly facilitating synapses that selectively transmit[48] the high-frequency, large-amplitude somnogenic bursts we observe. Alternatively, because action selection is an inherently competitive winner-take-all process, it may be sufficient for dFBNs to alter the probability that inaction is favored among competing options and let the internal architecture of the fan-shaped body[15] secure the exclusivity of the choice.

METHODS

Drosophila strains and culture. Flies were grown on media of cornmeal (62.5 g l^{-1}), inactive yeast powder (25 g l^{-1}), agar (6.75 g l^{-1}), molasses (37.5 ml l^{-1}), propionic acid (4.2 ml l^{-1}), tegosept (1.4 g l^{-1}), and ethanol (7 ml l^{-1}) under a 12 h light:12 h dark cycle at 25 °C in ~60% relative humidity, unless stated otherwise. To prevent the undesired activation of optogenetic actuators or the photoconversion of all-*trans* retinal by ambient light, flies expressing CsChrimson and their controls were reared and housed in constant darkness and transferred to food supplemented with 2 mM all-*trans* retinal (Molekula) in DMSO, or to DMSO vehicle only, 2 days before the optical stimulation experiments, at an age of 1–3 days post eclosion. Carriers of the *hs-FLP* transgene[49] were cultivated at 18 ˚C and placed on retinal-supplemented food for 5 days before optogenetic stimulation experiments.

Driver lines[50,51] *R23E10-GAL4* and *R23E10-LexA*, the repressor line *VGlut-3xGAL80*[52], and the split-GAL4 hemidrivers[52-55] *R23E10-DBD*, *VGlut-AD*, and *Gad1-AD* were used in the indicated combinations to target dFBNs[2] or other constituents of the *R23E10-GAL4* pattern at increasingly fine genetic resolution; *R69F08-GAL4* labelled R5 ring neurons of the ellipsoid body[37,50]. Effector transgenes encoded fluorescent markers for neuroanatomy (*UAS-6xEGFP*[56], *lexAop-GFP*[57], *UAS-tdTomato*[51], *UAS-mCD4::tdTomato*[58], *UAS-myrRFP*) or the labelling of synaptic active zones[41] (*lexAop-GFP*;*UAS-STaR*); the Ca^{2+} sensor[59,60] GCaMP6f; the glutamate[61] or dopamine[62] sensors iGluSnFR(A184V) or $GRAB_{DA2m}$, respectively; the optogenetic actuator[63] CsChrimson[64]; cassettes[18] for the mutually exclusive expression of green fluorescence (CD8::GFP or GCaMP6f) or CsChrimson::tdTomato after the FLP-mediated excision[49] of a transcriptional terminator; or RNAi constructs for interference with the expression of *VGlut* (4 independent transgenes[65,66]).

Sleep measurements, sleep deprivation, and optogenetic induction of sleep. Female flies aged 2–4 days were individually inserted into 65-mm glass tubes containing food reservoirs, loaded into the Trikinetics *Drosophila* Activity Monitor system, and housed under 12 h light:12 h dark conditions at 25 °C in ~60% relative humidity. Flies were allowed to habituate for one day before sleep was averaged over two consecutive recording days. Periods of inactivity lasting >5 minutes were classified as sleep[67,68] (Sleep and Circadian Analysis MATLAB Program[69]). Immobile flies (< 2 beam breaks per 24 h) were manually excluded.

Rebound sleep was quantified after sleep deprivation between zeitgeber times 12 and 24. An Ohaus Vortex Mixer stacked with Trikinetics monitors produced horizontal circular motion stimuli with a radius of ~1 cm at 25 Hz for 2 s; stimulation periods were randomly normally distributed within 20-s bins. A cumulative sleep loss plot was calculated for each individual by comparing the percentage of sleep lost during overnight sleep deprivation to the immediately preceding unperturbed night. Only flies losing >95% of baseline sleep were included in the analysis. Individual sleep rebound was quantified by normalizing the difference in sleep amount between rebound and baseline days to baseline sleep.

To deprive flies of sleep before functional imaging experiments, females with chronic imaging windows (see below) were inserted into Trikinetics monitors. The monitors were stacked on a spring-loaded platform, which was slowly tilted by an electric motor, released, and allowed to snap back to its original position[70]. The mechanical cycles lasted 10 s and were repeated continuously, beginning at zeitgeber time 12. Starting the next morning, flies were randomly selected from monitors, cold-anaesthetized for 5–10 minutes, head-fixed under the two-photon microscope, and allowed to recover for ≥25 minutes before imaging. Control flies were treated identically but allowed to sleep *ad libitum*. The same method of sleep deprivation, between zeitgeber times 12 and 24, was applied to females without chronic imaging windows before the quantification of BRP::V5 (synaptic tagging with recombination[41] or STaR).

In photostimulation experiments, female flies expressing CsChrimson in dFBNs were individually inserted into 65 mm glass tubes and loaded into a custom array[17] of light-tight chambers with high-power 630-nm LEDs (Multicomp OSW-4388). The apparatus was operated in a temperature-controlled incubator (Sanyo MIR-154) at 25 ˚C. For movement tracking, the chambers were continuously illuminated from below using low-power infrared (850 nm) LEDs and imaged from above with a high-resolution CMOS camera (Thorlabs DCC1545M) equipped with a long-pass filter (Thorlabs, FEL800nm) to reject stimulation light pulses, which lasted 3 ms and delivered ~28 mW cm^{-2} of optical power. A virtual instrument written in LabVIEW (National Instruments) extracted real-time position data from video images. Periods of inactivity lasting ≥5 minutes were classified as sleep. Flies that had been continuously immobile for 29.5 min per 30-min bin during ≥2 consecutive hours before the end of the experiment were excluded from the analysis, beginning with the hour preceding the onset of immobility.

Two-photon imaging. Females aged 1–3 days were implanted with chronic imaging windows[71,72] 2–3 days before the experiment. Unless otherwise stated (Supplementary Table 1), surgical openings created by removing cuticle, adipose tissue, and trachea were sealed with a thin layer of translucent UV-curable epoxy glue (Norland NOA13825; Opticure 2000 UV lamp, Norland) in a custom chamber perfused with CO_2 to avoid O_2 inhibition of the curing process, which lasted <45 s. The adhesive stabilized the brain, had a refractive index matched to that of water, and lacked any detectable adverse effects—including effects on sleep—after flies had recovered from cold and CO_2 anaesthesia. Flies were housed singly for 2–3 days after the procedure and were subsequently head-fixed to a custom mount with eicosane (Sigma) and imaged on a Movable Objective Microscope with resonant scanners (MOM, Sutter Instruments) controlled through ScanImage software (Vidrio Technologies). For sleep deprivation before imaging, experimental flies and their controls were placed into Trikinetics monitors 1–2 days after the implantation of the window.

Only healthy flies in which the adhesive effectively suppressed brain movements were imaged. Fluorophores were excited by a Mai Tai DeepSee Ti:sapphire laser (Spectra Physics model eHP DS; centre wavelength of 930 nm). A Pockels cell (302RM, Conoptics) kept the power at the specimen <15 mW (ThorLabs PM100D power meter console with ThorLabs S370C sensor head). Emitted photons were collected by a 20×/1.0 NA water immersion objective (W-Plan-Apochromat, Zeiss), split into green and red channels by a dichromatic mirror (Chroma 565dcxr) and bandpass filters (Chroma ET525/70m-2p and Chroma ET605/70m, respectively), and detected by GaAsP photomultiplier tubes (H10770PA-40 SEL, Hamamatsu Photonics). If simultaneous optogenetic stimulation was performed, an alternative bandpass filter (Semrock BrightLine FF01-520/60-25) was present in the green emission path. Photocurrents were passed through high-speed amplifiers (HCA-4M-500K-C, Laser Components) and custom-designed integrator circuits to maximize the signal-to-noise ratio. The objective was mounted on a MIPOS piezo actuator (PiezoSystemJena) controlled through ScanImage. Supplementary Table 1 lists the number of imaging planes, their axial distances, numbers of pixels, acquisition rates, and additional parameters for each experiment.

For optogenetic stimulation, a 625-nm LED (M625L3, ThorLabs) controlled by a dimmable LED driver (LEDD1B, ThorLabs) delivered ~0.5–25 mW cm^{-2} of optical power through a bandpass filter (Semrock BrightLine FF01-647/57-25) to the head of the fly. The voltage steps controlling the LED driver were recorded in a separate imaging channel for post-hoc alignment.

To deliver arousing stimuli, an 808-nm laser diode (Thorlabs L808P500MM) was mounted on a temperature-controlled heat sink (ThorLabs TCDLM9 with ThorLabs TED200C controller) and aimed at the abdomen of a fly standing or walking on a 6-mm polystyrene ball supported by a stream of air (0.3 l min^{-1}). The diode was restricted to a maximal output of 50 mW by a ThorLabs LDC210C laser diode controller. Rotations of the spherical treadmill were recorded by a GuppyPro camera equipped with a magnification lens and a Semrock FF01-647/57-50 bandpass filter at a mean acquisition rate of 22.80 Hz. The treadmill was dimly illuminated by a red LED through a bandpass filter (Semrock BrightLine FF01-647/57-25). Forward and turning velocities were computed by a custom MATLAB script (Jan Kropf, C.B.T., G.M., in preparation). Movement and imaging traces were aligned post hoc using simultaneously recorded voltage steps as time stamps.

For focal dopamine application, patch pipettes (~10 MΩ) containing 10 mM dopamine in extracellular solution were positioned near the dFBN dendritic tuft[6]. A TTL-controlled voltage step triggered dopamine delivery by a PDES-02DX pneumatic drug ejection system (npi electronic GmbH). Voltage steps were recorded in ScanImage for post-hoc alignment. Movement artefacts were controlled for by titrating the ejection pressure to 10–25 kPa and recording mCD4::tdTomato fluorescence in a separate imaging channel.

Functional imaging data were analysed using custom code in MATLAB. Rectangular regions of interest (ROIs) containing dFBN processes or irregularly shaped ROIs following the contours of dFBN somata or axons were manually drawn, along with a background ROI positioned on a non-fluorescent brain area, and time series of mean fluorescence intensities were extracted from two-photon image stacks. Following the subtraction of the average intensity of the background time series, ΔF/F curves were computed as $\Delta F_t/F^0_t = (F_t - F^0_t)/ F^0_t$, where F_t is the raw fluorescence intensity in frame t. For event-aligned analyses (i.e., GCaMP transient onset, optogenetic stimulation, or arousing heat), F^0_t was the mean fluorescence in a given time window before the event, as noted in figure legends. To correct for motion during pharmacological dopamine applications, normalized changes in green-to-red ratios (ΔR/R) were computed as $\Delta R_t/R_0 = (R_t - R_0)/ R_0$, where R_t is the element-wise ratio between background-subtracted GCaMP and mCD4::tdTomato signals and R_0 is the mean ratio 40 s before dopamine application.

For measurements of spontaneous dFBN activity, the time-varying baseline fluorescence F^0_t was obtained as the 10^{th} percentile of a symmetric sliding window of F_t, spanning 501 frames (~34 s). The resulting ΔF/F traces were smoothed with an 8-element Gaussian sliding window. GCaMP

transients were detected as peaks in the low-pass filtered (15-element Gaussian sliding window) time derivative of the ΔF/F trace; the amplitudes of transients were defined as the maximum within the 15 frames following the maximal rise of ΔF/F. Interhemispheric cross-correlations were computed on the normalized time derivative of the traces, which eliminates slow trends in the signal but captures the time course of dFBN bursts (Fig. 1f).

The blinded extraction of ROIs required some exclusions because of low signal-to-noise ratios. ROIs were excluded automatically from further analysis if their background-subtracted mean GCaMP fluorescence failed to exceed the standard deviation of a comparable background signal by 20-fold (raw traces) or 45-fold (smoothed traces). The baseline fluorescence of most ROIs easily passed these thresholds; with mean GCaMP fluorescence exceeding the standard deviation of background noise by factors of 87 (raw traces) or 183 (smoothed traces). In addition, where several focal planes of the same hemisphere were imaged, signals were screened for multiple representations of the same cell(s) by computing pairwise correlations between ROIs at different focal depths. Only the ROI showing the largest fluorescence intensity was retained if the correlation coefficient exceeded 0.85 for dendritic ROIs and 0.5 for somatic ROIs; in the latter case we confirmed by visual inspection that redundant ROIs covered the same somata. In $GRAB_{DA2m}$ experiments, the ROI displaying the highest response to the first heat shock was selected automatically for further analysis.

To relate GCaMP signals recorded simultaneously in the left and right dendrites and axons, linear regression models using the dendritic ΔF/F traces as predictor variables of the axonal traces were fit in MATLAB. Model performance was evaluated by 5-fold cross-validation.

Because Ca^{2+} diffuses into dFBN somata through the long, thin necks of dendrites and axons, somatic GCaMP signals are temporally low-pass filtered versions of signals recorded in the neuropil. This made an exhaustive characterization and classification of activity patterns of the dFBN ensemble (whose members could be resolved only in cell body images) impossible. Our analysis therefore focused on the distinction of pacemaker-like activity, which was readily detectable, from all other forms of activity. ΔF/F traces of individual somata were used to compute the peak signal power between 0.25 and 2 Hz; a prominent periodicity in the autocorrelogram with a wide amplitude swing during the first period was diagnostic of rhythmic dFBNs.

Electrophysiology. Female flies were head-fixed to a custom mount with eicosane (Sigma) or soft thermoplastic wax (Agar Scientific). A surgical window was cut into the cuticle; adipose tissue,

trachea, and the perineural sheath were removed; and the brain was superfused with carbogenated extracellular solution (95% O_2 – 5% CO_2, pH 7.3, 275 mOsm) containing (in mM) 103 NaCl, 3 KCl, 5 TES, 8 trehalose, 10 glucose, 7 sucrose, 26 $NaHCO_3$, 1 NaH_2PO_4, 1.5 $CaCl_2$, 4 $MgCl_2$. The GFP- or GCaMP- and mCD4::tdTomato-labelled somata of dFBNs were visualized using 20×/1.0 NA (W-Plan-Apochromat, Zeiss), 40×/0.8 NA, or 60×/1.0 NA water immersion objectives (LUMPLFLN40XW or LUMPLFLN60XW, Olympus) and targeted with borosilicate glass electrodes (8–11 MΩ) filled with internal solution (pH 7.3, 265 mOsM) containing (in mM): 10 HEPES, 140 potassium aspartate, 1 KCl, 4 MgATP, 0.5 Na_3GTP, 1 EGTA. Signals were acquired at room temperature in current-clamp mode with a MultiClamp 700B amplifier (Molecular Devices), lowpass-filtered at 5–20 kHz, and sampled at 10–50 kHz using an Axon Digidata 1440 digitizer controlled through pCLAMP 10.5 (Molecular Devices) or a Power1401-3A data acquisition interface controlled through Signal (Cambridge Electronic Design Ltd.).

For simultaneous whole-cell patch-clamp recording and two-photon imaging, a TTL-gated voltage signal was recorded in pClamp and ScanImage for the post-hoc alignment of electrophysiology and imaging data. Simultaneously recorded membrane voltages were compared with GCaMP fluorescence time series at the soma (9 of 10 cells); in one cell, Ca^{2+} signals were imaged in dendrites. The ΔF/F curve was computed as $\Delta F_t/F^0_t = (F_t - F^0_t)/ F^0_t$, where F_t was the raw fluorescence trace and the time-varying baseline fluorescence F^0_t was obtained as a 300-element (~5 s) moving average of F_t. The imaging time series was z-score-normalized and linearly interpolated and patch-clamp recordings were down-sampled, so that both signals had the same temporal resolution of 2 kHz; the resulting traces were aligned to the TTL time stamp. The momentary firing rate (or peri-event time histogram, PETH) was computed in 100-ms bins and used to create a predictor matrix for the estimation of the GCaMP impulse response from the interpolated and aligned imaging trace, which was smoothed using a 150 ms moving average and then downsampled to the same frame rate as the predictor matrix (10 Hz). The resolution of 10 Hz was chosen to control zero inflation in the predictor matrix (i.e., the number of time bins without spikes in the PETH) and reduce the number of coefficient weights to be fitted to 20 for a 2-s long impulse response. Model performance was evaluated by estimating the individual GCaMP impulse response functions of all 10 cells by linear regression and predicting the Ca^{2+} signal of each dFBN from its spiking record, using the normalized impulse response derived from the other 9 cells. Coefficients of determination (R^2) were obtained from the maximum cross-correlations between normalized and predicted imaging data.

In studies of inter-dFBN connectivity, low basal expression of the *hsFLP* transgene, without additional heat shock, was sufficient to produce recombination events[18,49] whose visible sign was a mosaic of green and red fluorescent dFBNs (Supplementary Fig. 3c). The presence of both dFBN populations was confirmed by live microscopy before each experiment. CsChrimson-expressing cells were stimulated with a 630-nm LED (Multicomp OSW-4388) controlled by a TTL-triggered dimmable LED driver (Recom RCD-24-0.70/W/X3) and focused on the fly's head with a mounted 60-mm lens (Thorlabs). The light source delivered 11–80 mW cm^{-2} of optical power. Where indicated, 1 μM tetrodotoxin (TTX) was perfused into the bath to probe for monosynaptic connections[18,73]. Data were analysed with custom procedures, using the NeuroMatic package (http://neuromatic.thinkrandom.com) in Igor Pro (WaveMetrics).

Confocal imaging. Single-housed females aged 6 days post eclosion were dissected at zeitgeber time 0. For the quantification of BRP::V5, experimental and control samples were processed in parallel, following *ad libitum* sleep or 12 h of sleep deprivation. Nervous systems were fixed for 20 min in 0.3% (v/v) Triton X-100 in PBS (PBST) with 4% (w/v) paraformaldehyde, washed five times with PBST, and incubated sequentially at 4 °C in blocking solution (10% goat serum in 0.3% PBST) overnight, with primary antibodies in blocking solution for 2–3 days, and with secondary antibodies in blocking solution for two days. The primary antibodies included mouse nc82 anti-BRP (1:10, Developmental Studies Hybridoma Bank), mouse anti-V5 (1:400, ThermoFisher), chicken anti-GFP (1:1000 or 1:500 for STaR, AbCam), and mouse anti-GFP (1:50 for GCaMP, ThermoFisher); the secondary antibodies were goat anti-Mouse Alexa Fluor 488 (1:1000, ThermoFisher), goat anti-Chicken Alexa Fluor 488 (1:1000 or 1:500 for STaR, ThermoFisher), and goat anti-Mouse Alexa Fluor 633 (1:500, ThermoFisher). The samples were washed five times with blocking solution before and after the addition of secondary antibodies, mounted in Vectashield, and imaged on a Leica TCS SP5 confocal microscope with an HCX IRAPO L 25×/0.95 water immersion objective. Only anatomically intact specimens from live flies (at the point of dissection) were analysed.

Connectome analysis. The hemibrain v1.2.1 connectome[74] was accessed in neuPrint+ (ref. [75]). Connectivity matrices were computed and analysed in MATLAB, omitting all diagonal entries (number of autapses, which were uniformly zero). An index of network density was computed as the number of observed edges (dFBN-to-dFBN connections) divided by the number of all possible edges in the graph. Measures of connection symmetry were obtained by correlating the weighted connectivity matrix with its transpose, and comparing the original directed with an undirected graph, which was created as the mean of the weighted connectivity matrix with its transpose. Instances of

unidirectional connections formed by one synapse were assigned a mean of 1 in the undirected graph. Non-zero entries above the diagonal in the connectivity matrix of the undirected graph are binned in the histogram of Supplementary Fig. 2a.

Quantification and statistical analysis. Imaging and behavioral data were analysed in MATLAB and Prism 10 (GraphPad). All null hypothesis tests were two-sided. To control type I errors, *P*-values were adjusted to achieve a joint α of 0.05 at each level in a hypothesis hierarchy; multiplicity adjusted *P*-values are reported in cases of multiple comparisons at one level. Group means were compared by *t* test, one-way ANOVA, two-way repeated-measures ANOVA, or mixed-effects models, as stated, followed by planned pairwise analyses using Holm-Šidák's multiple comparisons test. Repeated-measures ANOVA and mixed-effect models used the Geisser-Greenhouse correction. Where the assumption of normality was violated (as indicated by D'Agostino-Pearson test), group means were compared by Mann-Whitney test or Kruskal-Wallis ANOVA, followed by Dunn's multiple comparisons test, as indicated.

The investigators were blind to sleep history, zeitgeber time, the inclusion or exclusion of dietary retinal, and/or genotype during the selection of ROIs and background regions in functional imaging and STaR experiments in Fig. 1a, Fig. 2, Fig. 3e, i, Fig. 4, Fig. 5g, Fig, 6a, b, and Supplementary Fig. 5 but not otherwise. Sample sizes in behavioral experiments (typically n=32 flies per genotype) were chosen to detect 2-h differences in daily sleep with a power of 0.9. All behavioral experiments were run at least three times, on different days and with different batches of flies. The figures show pooled data from all replicates.

Modelling. We studied a model of two dFBNs (one in the left and one in the right hemisphere) with reciprocal inhibitory connections. Each dFBN was driven by 20 presynaptic units whose spike trains were inhomogeneous Poisson processes; the rates of these Poisson processes were subject to feedback modulation by the summed inhibitory output of both dFBNs. The architecture of the model is based on anatomical and functional evidence of recurrent connectivity between R5 neurons of the ellipsoid body (corresponding to the presynaptic units) and dFBNs[17,37]. R5 neurons provide indirect excitation to dFBNs[37], whose inhibitory activity in turn diminishes (again via indirect connections[17]) the excitatory drive R5 neurons provide. Our minimal model recapitulates the basic feedback logic of the circuit but simplifies it by replacing indirect with direct connections and relying on a biphasic filter (rather than explicit conductances) to model hyperpolarization and hyperpolarization-induced escape.

Sleep loss-dependent changes were incorporated via three model parameters, as suggested by empirical data (Supplementary Fig. 5b). First, dFBNs in sleep-deprived flies increase their intrinsic excitability[2]. This was modelled as a shortening of the refractory period following a dFBN spike. Second, R5 neurons display higher firing rates and larger presynaptic active zones after sleep deprivation[37] (Supplementary Fig. 5a). This was modelled as an increase in the rate of the Poisson units. Third, dFBN output synapses weaken after sleep loss (Fig. 6a, b). This was modelled as a decrease in the connection weight between dFBNs and the Poisson units.

A spike response model[76] described the membrane potential $v_j(t)$ of each dFBN in discrete 1-ms time steps as a linear sum of a resting membrane potential (v_{rest}) of –50 mV, excitatory postsynaptic potentials (EPSPs) due to input from n = 20 Poisson units, spike after-hyperpolarization, and the inhibitory postsynaptic potentials (IPSPs) and postinhibitory rebound elicited by the contralateral dFBN:

$$v_j(t) = v_{rest} + \sum_{i=1}^{n} \sum_{t_i \in S_i^{in}} \varepsilon(t - t_i) + \sum_{t_j \in S_j^{dFB}} \eta(t - t_j) + \sum_{t_k \in S_k^{dFB}} w_{jk} \cdot \zeta(t - t_k) . \quad (1)$$

S_i^{in}, S_j^{dFB}, and S_k^{dFB} are sets of spike times (t_i, t_j, and t_k) of the i^{th} input unit, dFBN$_j$, and the contralateral dFBN$_k$.

EPSPs had a rise time constant τ_1 of 7 ms and a decay time constant τ_2 of 150 ms; their amplitude ε was scaled to a peak of 0.75 mV:

$$\varepsilon(t - t_i) = \exp\left(-\frac{t-t_i}{\tau_1}\right) - \exp\left(-\frac{t-t_i}{\tau_2}\right) . \quad (2)$$

The post-spike hyperpolarization was defined as

$$\eta(t - t_j) = \eta_0 \cdot \exp\left(-\frac{t - t_j}{\tau_3}\right) \quad (3)$$

with τ_3 = 300 ms and $\eta_0 = -6$ mV.

The time course of an IPSP and its postinhibitory rebound was encapsulated by a biphasic filter

$$\zeta(t - t_k) = \exp\left(-\frac{t-t_k}{\tau_4}\right) - \rho \cdot \exp\left(-\frac{t-t_k}{\tau_5}\right) + \exp\left(-\frac{t-t_k}{\tau_6}\right) \quad (4)$$

with τ_4 = 450 ms, τ_5 = 225 ms, τ_6 = 56 ms, and ρ = 2. The filter was normalized and weighted by the amplitude $w_{jk} = w_{kj} =$ 8 mV for each contralateral dFBN spike (Eq. 1).

Spike initiation by dFBNs was deterministic. If a time-varying voltage threshold $\vartheta(t)$ was crossed, an action potential was initiated (modelled as the addition of a 20-mV impulse to the current threshold value). To incorporate refractoriness, this deterministic threshold was a function of spiking history

$$\vartheta(t) = \vartheta_0 + \sum_{t_j \in S_j^{dFB}} \theta(t - t_j), \quad (5)$$

where the baseline spiking threshold ϑ_0 was –45 mV and

$$\theta(t - t_j) = \theta_0 \cdot \exp\left(-\frac{t - t_j}{\tau_7}\right). \quad (6)$$

The decay time constant τ_7 was 30 ms in rested and 15 ms in sleep-deprived conditions, respectively, to account for variation in the intrinsic excitability of dFBNs[2] (Supplementary Fig. 5b). θ_0 was 400 mV.

The spike trains of 20 input units per dFBN were modelled as inhomogeneous Poisson processes with a basal rate ω_0 of 30 in rested and 60 in sleep-deprived flies (Supplementary Fig. 5b), matching empirical firing rate increases in R5 neurons[37]. Inhibitory feedback from the summed output of both dFBNs reduced the momentary Poisson rate $\omega(t)$ according to

$$\omega(t) = \psi(t - t_j) + \psi(t - t_k) + \omega_0, \quad (7)$$

where

$$\begin{aligned} \psi(t - t_j) &= -\exp\left(-\frac{t-t_j}{\tau_8}\right) + \exp\left(-\frac{t-t_j}{\tau_9}\right) \text{ and} \\ \psi(t - t_k) &= -\exp\left(-\frac{t - t_k}{\tau_8}\right) + \exp\left(-\frac{t - t_k}{\tau_9}\right) \end{aligned} \quad (8)$$

with τ_8 = 7 ms and τ_9= 1000 ms. The amplitude of ψ was normalized and scaled by a variable output weight reflecting the observed presynaptic plastic changes in dFBNs; sleep deprivation was modelled as a 50% reduction in the postsynaptic response amplitude (Supplementary Fig. 5b). $\omega(t)$ was restricted to positive values.

Calcium imaging experiments were simulated by convolving the momentary firing rates of model dFBNs in 100-ms bins with the GCaMP impulse response function estimated from simultaneous patch-clamp recordings. Data were z-score normalized.

Acknowledgments

We thank E. Agnes for discussions of the spike-response model and K. Golic, Y.-N. Jan, V. Jayaraman, D. Kim, T. Lee, Y. Li, L. Looger, G. Rubin, R. Stowers, J. Truman, B. White, L. Zipursky, the Bloomington Stock Center, the Vienna *Drosophila* Resource Center, and the Transgenic RNAi Project (TRiP) for flies. This work was supported by grants from the European Research Council (832467) and Wellcome (209235/Z/17/Z and 106988/Z/15/Z) to G. M. P.S.H. was an Erwin Schrödinger Fellow of the Austrian Science Fund (J 4060); R. S. held a Wellcome Four-Year PhD Studentship in Basic Science (215200/Z/19/Z).

Author contributions

P.S.H. performed and analysed all functional imaging studies, developed the dFBN model, analysed connectomic data with R.S., and wrote an initial manuscript draft; R.S. performed and analysed all neuroanatomical and behavioral and some imaging experiments; E.V. and H.O.R. obtained electrophysiological recordings; C.B.T. developed instrumentation; R.B. generated fly strains. P.S.H., R.S., and G.M. designed the study, interpreted the results, and prepared the manuscript. G.M. devised and directed the research and wrote the final version of the paper.

Correspondence and requests for materials should be addressed to G.M. (gero.miesenboeck@cncb.ox.ac.uk).

References

1. Donlea, J. M., Thimgan, M. S., Suzuki, Y., Gottschalk, L. & Shaw, P. J. Inducing sleep by remote control facilitates memory consolidation in Drosophila. *Science* **332**, 1571-1576 (2011).
2. Donlea, J. M., Pimentel, D. & Miesenböck, G. Neuronal machinery of sleep homeostasis in Drosophila. *Neuron* **81**, 860-872 (2014).
3. Kempf, A., Song, S. M., Talbot, C. B. & Miesenböck, G. A potassium channel β-subunit couples mitochondrial electron transport to sleep. *Nature* **568**, 230-234 (2019).
4. Sarnataro, R., Velasco, C. D., Monaco, N., Kempf, A. & Miesenböck, G. Mitochondrial origins of the pressure to sleep. *Submitted.* (2024).
5. Rorsman, H. O. et al. Sleep pressure accumulates in a voltage-gated lipid peroxidation memory. *Submitted.* (2024).
6. Pimentel, D. et al. Operation of a homeostatic sleep switch. *Nature* **536**, 333-337 (2016).
7. Blake, H., Gerard, R. W. & Kleitman, N. Factors influencing brain potentials during sleep. *J Neurophysiol* **2**, 48-60 (1939).
8. McCormick, D. A. & Pape, H. C. Properties of a hyperpolarization-activated cation current and its role in rhythmic oscillation in thalamic relay neurones. *J Physiol* **431**, 291-318 (1990).
9. Brown, T. G. The intrinsic factors in the act of progression in the mammal. *Proc R Soc B* **84**, 308-319 (1911).
10. Satterlie, R. A. Reciprocal inhibition and postinhibitory rebound produce reverberation in a locomotor pattern generator. *Science* **229**, 402-404 (1985).
11. Marder, E. & Bucher, D. Central pattern generators and the control of rhythmic movements. *Curr Biol* **11**, R986-96 (2001).
12. Grillner, S. Biological pattern generation: The cellular and computational logic of networks in motion. *Neuron* **52**, 751-766 (2006).
13. McCarley, R. W. & Hobson, J. A. Neuronal excitability modulation over the sleep cycle: A structural and mathematical model. *Science* **189**, 58-60 (1975).
14. Fenk, L. A., Riquelme, J. L. & Laurent, G. Interhemispheric competition during sleep. *Nature* **616**, 312-318 (2023).
15. Hulse, B. K. et al. A connectome of the Drosophila central complex reveals network motifs suitable for flexible navigation and context-dependent action selection. *Elife* **10**, e66039 (2021).
16. Liu, W. W. & Wilson, R. I. Glutamate is an inhibitory neurotransmitter in the Drosophila olfactory system. *Proc Natl Acad Sci USA* **110**, 10294-10299 (2013).
17. Donlea, J. M. et al. Recurrent circuitry for balancing sleep need and sleep. *Neuron* **97**, 378-389.e4 (2018).
18. Vrontou, E. et al. Response competition between neurons and antineurons in the mushroom body. *Curr Biol* **31**, 4911-4922.e4 (2021).
19. Jones, J. D. et al. Regulation of sleep by cholinergic neurons located outside the central brain in Drosophila. *PLoS Biol* **21**, e3002012 (2023).
20. De, J., Wu, M., Lambatan, V., Hua, Y. & Joiner, W. J. Re-examining the role of the dorsal fan-shaped body in promoting sleep in Drosophila. *Curr Biol* **33**, 3660-3668.e4 (2023).
21. French, A. S., Geissmann, Q., Beckwith, E. J. & Gilestro, G. F. Sensory processing during sleep in Drosophila melanogaster. *Nature* **598**, 479-482 (2021).
22. Tabuchi, M. et al. Clock-generated temporal codes determine synaptic plasticity to control sleep. *Cell* **175**, 1213-1227.e18 (2018).
23. Gent, T. C., Bandarabadi, M., Herrera, C. G. & Adamantidis, A. R. Thalamic dual control of sleep and wakefulness. *Nat Neurosci* **21**, 974-984 (2018).
24. Loomis, A. L., Harvey, E. N. & Hobart, G. A. Cerebral states during sleep, as studied by human brain potentials. *J Exp Psychol* **21**, 127-144 (1937).

25. Steriade, M., McCormick, D. A. & Sejnowski, T. J. Thalamocortical oscillations in the sleeping and aroused brain. *Science* **262**, 679-85. (1993).
26. Achermann, P., Dijk, D. J., Brunner, D. P. & Borbély, A. A. A model of human sleep homeostasis based on EEG slow-wave activity: Quantitative comparison of data and simulations. *Brain Res Bull* **31**, 97-113 (1993).
27. Nitz, D. A., van Swinderen, B., Tononi, G. & Greenspan, R. J. Electrophysiological correlates of rest and activity in Drosophila melanogaster. *Curr Biol* **12**, 1934-1940 (2002).
28. Yap, M. H. W. et al. Oscillatory brain activity in spontaneous and induced sleep stages in flies. *Nat Commun* **8**, 1815 (2017).
29. Raccuglia, D. et al. Network-Specific synchronization of electrical slow-wave oscillations regulates sleep drive in Drosophila. *Curr Biol* **29**, 3611-3621.e3 (2019).
30. Raccuglia, D. et al. Coherent multi-level network oscillations create neural filters to favor quiescence over navigation in Drosophila. *bioRxiv* 2022.03.11.483976 (2022).
31. Liu, Q., Liu, S., Kodama, L., Driscoll, M. R. & Wu, M. N. Two dopaminergic neurons signal to the dorsal fan-shaped body to promote wakefulness in Drosophila. *Curr Biol* **22**, 2114-2123 (2012).
32. Ueno, T. et al. Identification of a dopamine pathway that regulates sleep and arousal in Drosophila. *Nat Neurosci* **15**, 1516-1523 (2012).
33. Saper, C. B., Chou, T. C. & Scammell, T. E. The sleep switch: Hypothalamic control of sleep and wakefulness. *Trends Neurosci* **24**, 726-731 (2001).
34. Goldman, M. S., Golowasch, J., Marder, E. & Abbott, L. F. Global structure, robustness, and modulation of neuronal models. *J Neurosci* **21**, 5229-5238 (2001).
35. Marder, E. Variability, compensation, and modulation in neurons and circuits. *Proc Natl Acad Sci U S A* **108 Suppl 3**, 15542-15548 (2011).
36. Morozova, E., Newstein, P. & Marder, E. Reciprocally inhibitory circuits operating with distinct mechanisms are differently robust to perturbation and modulation. *Elife* **11**, e74363 (2022).
37. Liu, S., Liu, Q., Tabuchi, M. & Wu, M. N. Sleep drive is encoded by neural plastic changes in a dedicated circuit. *Cell* **165**, 1347-1360 (2016).
38. Harrell, E. R., Pimentel, D. & Miesenböck, G. Changes in presynaptic gene expression during homeostatic compensation at a central synapse. *J Neurosci* **41**, 3054-3067 (2021).
39. Wagh, D. A. et al. Bruchpilot, a protein with homology to ELKS/CAST, is required for structural integrity and function of synaptic active zones in Drosophila. *Neuron* **49**, 833-844 (2006).
40. Kittel, R. J. et al. Bruchpilot promotes active zone assembly, Ca2+ channel clustering, and vesicle release. *Science* **312**, 1051-1054 (2006).
41. Chen, Y. et al. Cell-type-specific labeling of synapses in vivo through synaptic tagging with recombination. *Neuron* **81**, 280-293 (2014).
42. Weyhersmüller, A., Hallermann, S., Wagner, N. & Eilers, J. Rapid active zone remodeling during synaptic plasticity. *J Neurosci* **31**, 6041-6052 (2011).
43. Tononi, G. & Cirelli, C. Sleep and synaptic homeostasis: A hypothesis. *Brain Res Bull* **62**, 143-150 (2003).
44. Donlea, J. M., Ramanan, N. & Shaw, P. J. Use-dependent plasticity in clock neurons regulates sleep need in Drosophila. *Science* **324**, 105-108 (2009).
45. Gilestro, G. F., Tononi, G. & Cirelli, C. Widespread changes in synaptic markers as a function of sleep and wakefulness in Drosophila. *Science* **324**, 109-112 (2009).
46. Weiss, J. T. & Donlea, J. M. Sleep deprivation results in diverse patterns of synaptic scaling across the Drosophila mushroom bodies. *Curr Biol* **31**, 3248-3261.e3 (2021).

47. Huang, S., Piao, C., Beuschel, C. B., Zhao, Z. & Sigrist, S. J. A brain-wide form of presynaptic active zone plasticity orchestrates resilience to brain aging in Drosophila. *PLoS Biol* **20**, e3001730 (2022).
48. Lisman, J. E. Bursts as a unit of neural information: Making unreliable synapses reliable. *Trends Neurosci* **20**, 38-43 (1997).
49. Golic, K. G. & Lindquist, S. The FLP recombinase of yeast catalyzes site-specific recombination in the Drosophila genome. *Cell* **59**, 499-509 (1989).
50. Jenett, A. et al. A GAL4-driver line resource for Drosophila neurobiology. *Cell Rep* **2**, 991-1001 (2012).
51. Pfeiffer, B. D. et al. Refinement of tools for targeted gene expression in Drosophila. *Genetics* **186**, 735-755 (2010).
52. Diao, F. et al. Plug-and-play genetic access to Drosophila cell types using exchangeable exon cassettes. *Cell Rep* **10**, 1410-1421 (2015).
53. Luan, H., Peabody, N. C., Vinson, C. R. & White, B. H. Refined spatial manipulation of neuronal function by combinatorial restriction of transgene expression. *Neuron* **52**, 425-436 (2006).
54. Dionne, H., Hibbard, K. L., Cavallaro, A., Kao, J. C. & Rubin, G. M. Genetic reagents for making split-GAL4 lines in Drosophila. *Genetics* **209**, 31-35 (2018).
55. Lacin, H. et al. Neurotransmitter identity is acquired in a lineage-restricted manner in the Drosophila CNS. *Elife* **8**, e43701 (2019).
56. Shearin, H. K., Macdonald, I. S., Spector, L. P. & Stowers, R. S. Hexameric GFP and mCherry reporters for the Drosophila GAL4, Q, and LexA transcription systems. *Genetics* **196**, 951-960 (2014).
57. Lai, S. L. & Lee, T. Genetic mosaic with dual binary transcriptional systems in Drosophila. *Nat Neurosci* **9**, 703-709 (2006).
58. Han, C., Jan, L. Y. & Jan, Y. N. Enhancer-driven membrane markers for analysis of nonautonomous mechanisms reveal neuron-glia interactions in Drosophila. *Proc Natl Acad Sci U S A* **108**, 9673-9678 (2011).
59. Nakai, J., Ohkura, M. & Imoto, K. A high signal-to-noise Ca2+ probe composed of a single green fluorescent protein. *Nat Biotechnol* **19**, 137-141. (2001).
60. Chen, T.-W. et al. Ultrasensitive fluorescent proteins for imaging neuronal activity. *Nature* **499**, 295-300 (2013).
61. Marvin, J. S. et al. An optimized fluorescent probe for visualizing glutamate neurotransmission. *Nat Methods* **10**, 162-170 (2013).
62. Sun, F. et al. Next-generation GRAB sensors for monitoring dopaminergic activity in vivo. *Nat Methods* **17**, 1156-1166 (2020).
63. Zemelman, B. V., Lee, G. A., Ng, M. & Miesenböck, G. Selective photostimulation of genetically chARGed neurons. *Neuron* **33**, 15-22 (2002).
64. Klapoetke, N. C. et al. Independent optical excitation of distinct neural populations. *Nat Methods* **11**, 338-346 (2014).
65. Dietzl, G. et al. A genome-wide transgenic RNAi library for conditional gene inactivation in Drosophila. *Nature* **448**, 151-156 (2007).
66. Perkins, L. A. et al. The Transgenic RNAi Project at Harvard Medical School: Resources and validation. *Genetics* **201**, 843-852 (2015).
67. Hendricks, J. C. et al. Rest in Drosophila is a sleep-like state. *Neuron* **25**, 129-138 (2000).
68. Shaw, P. J., Cirelli, C., Greenspan, R. J. & Tononi, G. Correlates of sleep and waking in Drosophila melanogaster. *Science* **287**, 1834-1837 (2000).
69. Vecsey, C. G., Koochagian, C., Porter, M. T., Roman, G. & Sitaraman, D. Analysis of sleep and circadian rhythms from Drosophila Activity-Monitoring data using SCAMP. *Cold Spring Harb Protoc* (2024).

70. Shaw, P. J., Tononi, G., Greenspan, R. J. & Robinson, D. F. Stress response genes protect against lethal effects of sleep deprivation in Drosophila. *Nature* **417**, 287-291 (2002).
71. Grover, D., Katsuki, T. & Greenspan, R. J. Flyception: Imaging brain activity in freely walking fruit flies. *Nat Methods* **13**, 569-572 (2016).
72. Huang, C. et al. Long-term optical brain imaging in live adult fruit flies. *Nat Commun* **9**, 872 (2018).
73. Petreanu, L., Mao, T., Sternson, S. M. & Svoboda, K. The subcellular organization of neocortical excitatory connections. *Nature* **457**, 1142-1145 (2009).
74. Scheffer, L. K. et al. A connectome and analysis of the adult Drosophila central brain. *Elife* **9**, e57443 (2020).
75. Plaza, S. M. et al. neuOrint: An open access tool for EM connectomics. *Front Neuroinform* **16**, 896292 (2022).
76. Gerstner, W. & van Hemmen, J. L. Associative memory in a network of 'spiking' neurons. *Network* **3**, 139-164 (1992).

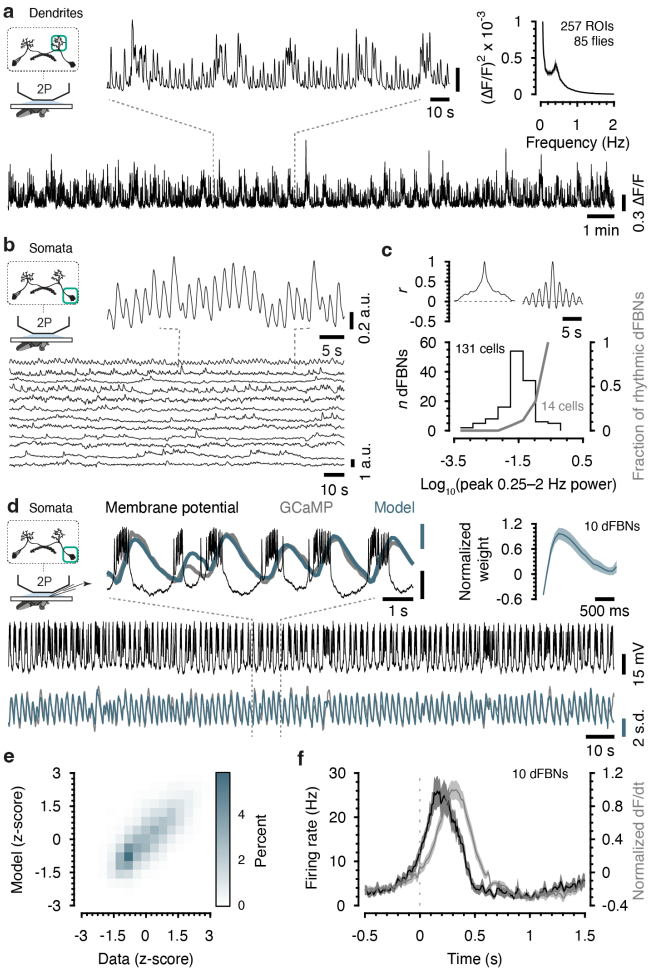

Figure 1 | A rhythmic subset of dFBNs generate slow-wave activity.

a, Imaging of dFBN dendrites. The example shows 180 s of a GCaMP trace spanning ~22 minutes (bottom) at expanded x- and y-scales on top. Top right, power spectrum. **b**, Simultaneous imaging of 12 dFBN somata in one hemisphere (intensity-normalized fluorescence). A portion of the uppermost trace is shown at expanded x- and y-scales on top. **c**, Top, GCaMP fluorescence autocorrelograms of the uppermost (right) and lowermost (left) dFBNs in **b**. Bottom, log-scaled distributions of 0.25–2 Hz power among 131 dFBNs in 17 hemispheres of 13 flies (black) and fraction of rhythmic dFBNs in each bin (gray). Prominent periodicity in the autocorrelogram with a wide amplitude swing during the first period was diagnostic of rhythmic dFBNs. **d**, Simultaneous imaging and patch-clamp recording from dFBN somata. Black, grey, and blue traces represent recorded voltages and z-score-normalized measured and predicted GCaMP traces, respectively, shown at expanded x- and y-scales on top (s.d., standard deviation). Lower end of voltage scale bars, –45 mV. Top right, normalized GCaMP impulse response. **e**, Two-dimensional histogram of measured vs. predicted GCaMP signals, color-coded according to the key on the right. R^2=0.54±0.21 (mean±s.d.). **f**, Firing rate (30-ms moving average, black) aligned to GCaMP transient onset, defined as the zero crossing of the first

derivative of the normalized fluorescence trace (gray). Data are means ± s.e.m. For imaging details see Supplementary Table 1.

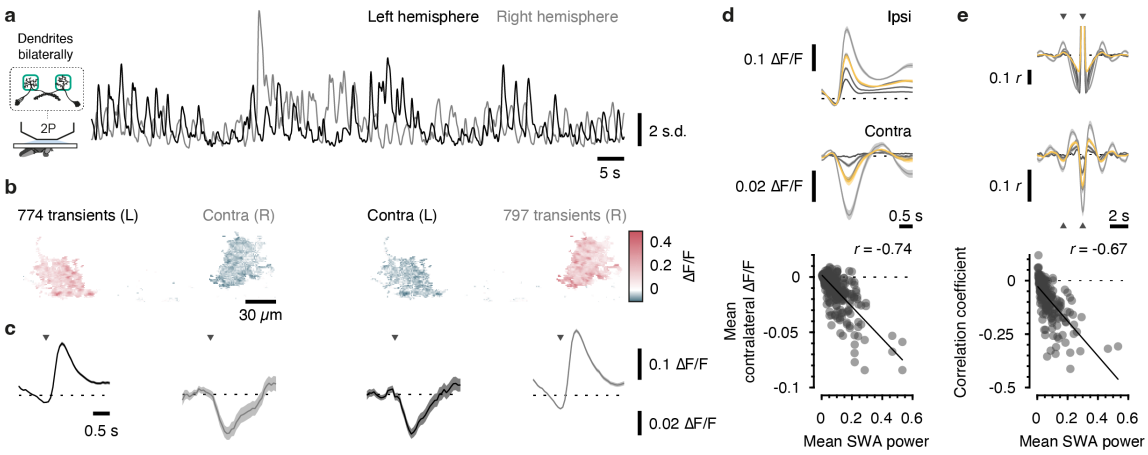

Figure 2 | Rhythmic dFBNs form a half-centre oscillator.

a, Simultaneous imaging of dFBN dendrites in both hemispheres. The example shows 100 s of z-score-normalized GCaMP traces spanning ~22 minutes. **b**, **c**, Ipsi- (red) and contralateral (blue) z-score-normalized fluorescence changes (**b**) and GCaMP traces (**c**) during transients in the left (L) and right (R) hemispheres (same fly as in **a**). Images in **b** depict mean ΔF/F in 10 frames (~700 ms) after transient onset vs. the preceding 15 frames; the images are thresholded for display and pseudocolored according to the key on the right. Ipsi- and contralateral GCaMP traces in **c** are plotted at different ΔF/F scales; arrowheads mark the onset of ipsilateral transients; dashed horizontal lines indicate ΔF/F = 0. **d**, **e**, Transient-aligned average ipsi- (top) and contralateral (centre) GCaMP traces (**d**) and their auto- and cross-correlograms (**e**) in the full dataset (*n*=60 flies; 208 ROIs; 201,484 transients). Shades of gray from dark to light show increasing quartiles of SWA power in both hemispheres; yellow traces represent population averages. Bottom, linear regression of mean contralateral ΔF/F (**d**) and interhemispheric correlation coefficients (**e**) vs. SWA power in both hemispheres. Shades of gray from dark to light show increasing quartiles of SWA power; yellow traces represent population averages. Correlograms are clipped near autocorrelation peaks; arrowheads indicate one period. Data are means ± s.e.m. For imaging details see Supplementary Table 1.

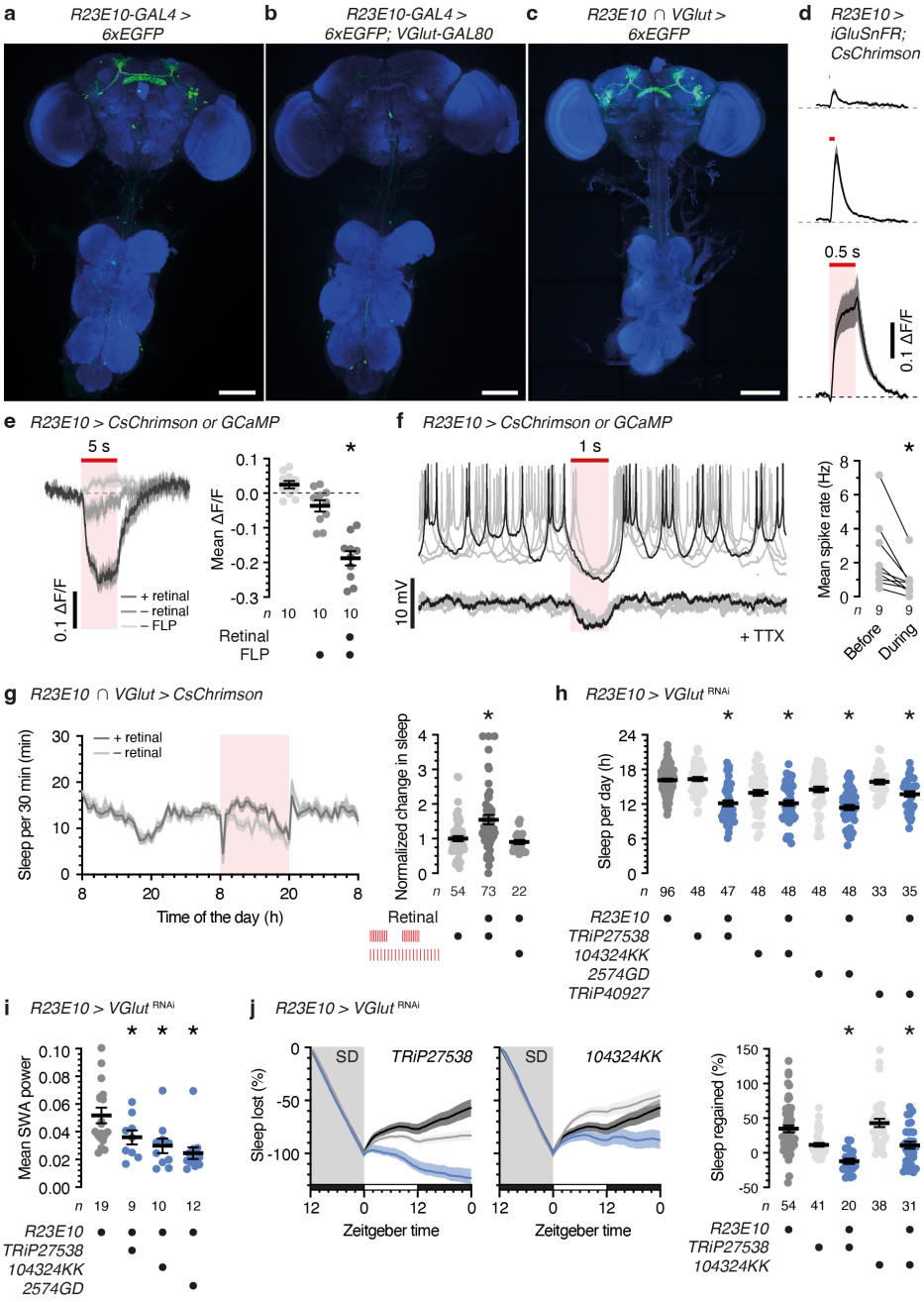

Figure 3 | dFBNs promote sleep via glutamate.

a, **b**, Maximum-intensity projections of brain and ventral nerve cord (VNC) of flies expressing 6xEGFP under the control of *R23E10-GAL4*, in the absence (**a**) or presence (**b**) of the transcriptional repressor VGlut-GAL80. **c**, Maximum-intensity projection of brain and VNC of a fly expressing 6xEGFP under the control of hemidrivers *vGlut-p65AD* and *R23E10-DBD* (*R23E10* ∩ *VGlut-GAL4*). **d**, Optogenetic stimulation of dFBNs expressing CsChrimson and iGluSnFR elicits glutamate release from axons (*n*=10 flies). Horizontal dashed lines at ΔF/F = 0. **e**, **f**, Imaging (**e**) and electrophysiological (**f**) demonstration of inhibition among non-overlapping dFBN populations expressing CsChrimson or a green fluorophore (GCaMP in **e**, mCD8::GFP in **f**) after FLP-mediated recombination. Somatic GCaMP fluorescence of CsChrimson-negative dFBNs declines during optogenetic stimulation of CsChrimson-positive dFBNs (**e**, *P*<0.0001, ANOVA). Optogenetic stimulation

of CsChrimson-positive dFBNs hyperpolarizes CsChrimson-negative (and mCD8::GFP-positive) dFBNs and suppresses spiking (**f**, *P*=0.0039, Wilcoxon test). Inter-dFBN inhibition persists in the presence of 1 µM tetrodotoxin (TTX). **g**, Sleep profiles (left) of flies expressing CsChrimson under the control of *R23E10* ∩ *VGlut-GAL4*, with or without retinal, before, during, and after optogenetic replay of SWA (time × retinal interaction: *P*<0.0001, retinal effect: *P*=0.0148, mixed-effects model). SWA, but not tonic stimulation at 10 Hz, increases sleep (right, *P*<0.0001, Kruskal-Wallis ANOVA) **h**–**j**, *R23E10-GAL4*-driven RNAi transgenes directed against VGlut reduce baseline sleep (**h**, *P*≤0.0077, Holm-Šídák test after ANOVA), average SWA power (**i**, genotype effect: *P*=0.0005, ANOVA), and the time courses and percentages of sleep rebound after deprivation (SD) (**i**, time x genotype interactions in left panels: *P*<0.0001, two-way ANOVA; genotype effect in right panel: *P*<0.0001, Kruskal-Wallis ANOVA). The normalized sleep increases of 3 flies in **g,** SWA power of one fly in **i**, and sleep rebound of one fly in **j** exceed the y-axis limits and are plotted at the top of the respective graphs; statistics are based on the actual values. Data are means ± s.e.m.; *n*, number of flies (**e, g**–**j**) or cells (**f**); asterisks, significant differences (*P*<0.05) in planned pairwise comparisons. For imaging details see Supplementary Table 1. For statistical details see Supplementary Table 2.

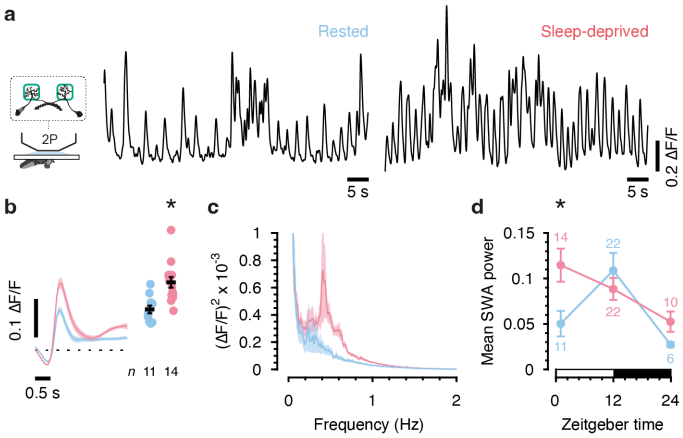

Figure 4 | dFBN slow-wave activity encodes sleep need.

a, Example GCaMP traces of dFBN dendrites at zeitgeber time 0–4, after unperturbed rest (blue) or sleep deprivation between zeitgeber times 12 and 24 (red). **b**, **c**, Sleep deprivation increases the average GCaMP transient (**b**, left), its peak amplitude (**b**, right, P=0.0028, Mann-Whitney test), and SWA power (**c**). **d**, Mean SWA power during the course of a day in rested (blue) and sleep-deprived flies (time × sleep history interaction: P=0.0228, mixed-effects model). Same dataset as in Fig. 1a and Fig. 2. Data are means ± s.e.m.; n, number of flies; asterisks, significant differences (P<0.05) in planned pairwise comparisons. For statistical details see Supplementary Table 1. For imaging details see Supplementary Table 1. For statistical details see Supplementary Table 2.

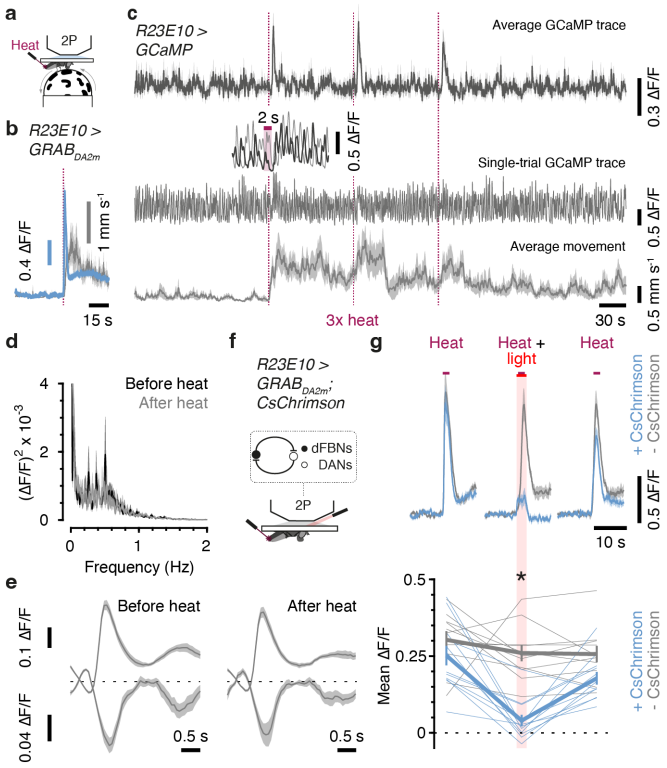

Figure 5 | SWA persists during arousal.

a, Movement tracking and imaging during the application of arousing heat. **b**, Heat (dashed carmine line) stimulates dopamine release onto dFBN dendrites expressing $GRAB_{DA2m}$ (blue) and locomotor bouts (gray) (*n*=9 flies). **c**, Dendritic GCaMP and locomotor traces before, during, and after three heat applications (dashed carmine lines). Top, cancellation of SWA in the average GCaMP trace (*n*=11 flies) reveals rebound responses aligned to the offset of heat. Lower end of scale bar, ΔF/F = 0. Centre, GCaMP trace of a single trial. Lower end of scale bar, ΔF/F = –0.15. Segments of GCaMP traces in both hemispheres during one heat application are shown at expanded x- and y-scales on top. Bottom, average locomotor speed. Lower end of scale bar, 0 mm s^{-1}. **d**, **e**, Power spectra (**d**) and transient-aligned average ipsi- (top) and contralateral (bottom) GCaMP traces (**e**) in 8 flies where both hemispheres were imaged, during 140-s windows before and after the application of heat. **f**, Optogenetic stimulation of dFBNs during the application of heat probes for an inhibitory flip-flop arrangement of dFBNs and arousing dopaminergic neurons (DANs). **g**, Light during heat application inhibits dopamine release onto CsChrimson-positive (blue, *n*=12 flies) but not CsChrimson-negative dFBNs (gray, *n*=11 flies). Top, example traces of three applications of heat (spaced 30 minutes apart) to the same flies. Traces were smoothed with a 5-element (~300 ms) moving-average filter for display. Bottom, dFBN stimulation reduces mean $GRAB_{DA2m}$ fluorescence during heat application (heat × CsChrimson interaction: *P*=0.0017, two-way ANOVA). Thin lines, individual flies; thick lines, population averages. Data are means ± s.e.m.; asterisk, significant difference (*P*<0.05) in a planned pairwise comparison. For imaging details see Supplementary Table 1. For statistical details see Supplementary Table 2.

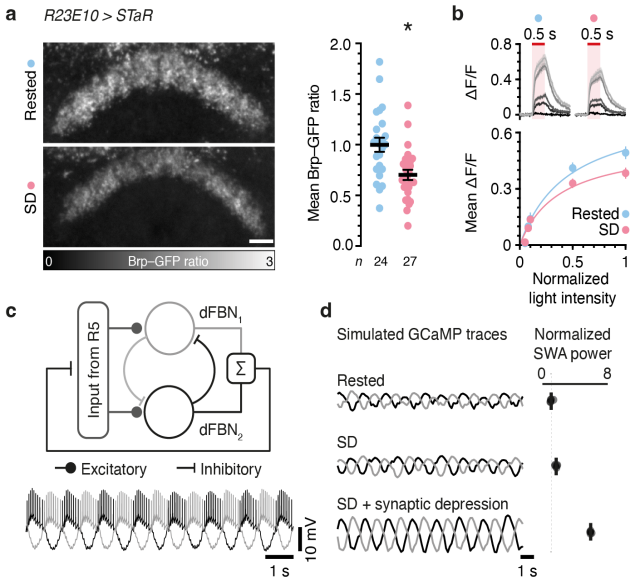

Figure 6 | Efferent dFBN synapses depress after sleep deprivation.

a, Summed-intensity projections of V5-tagged endogenous BRP in dFBN axons coexpressing mCD8::GFP. Emission ratios are intensity-coded according to the key at the bottom and decrease after sleep deprivation (SD) (P=0.0009, t test). Scale bar, 10 µm. **b**, Sleep deprivation reduces glutamate release elicited by optogenetic stimulation of dFBNs (light intensity × sleep history interaction: P<0.0001, two-way ANOVA). Top, iGluSnFR traces (n=11 rested and 12 SD flies). Shades of gray from dark to light show increasing light intensities normalized to peak (25 mW cm^{-2}). Bottom, mean iGluSnFR ΔF/F during illumination in rested (blue) and sleep-deprived flies (red) as functions of light intensity. Data are fitted by saturation hyperbolas. **c**, Minimal model of two dFBNs with reciprocal inhibitory connections in a simplified feedback circuit with a pool of excitatory Poisson units. Top, model schematic. Bottom, simulated voltage traces of dFBNs color-coded as on top. **d**, Simulated GCaMP traces (left) and mean SWA power (right) at baseline and after sleep deprivation, in the absence and presence of plastic feedback connections with Poisson units (n=5 simulations). Data are means ± s.e.m.; asterisk, significant difference (P<0.05) in a planned pairwise comparison. For imaging details see Supplementary Table 1. For statistical details see Supplementary Table 2.

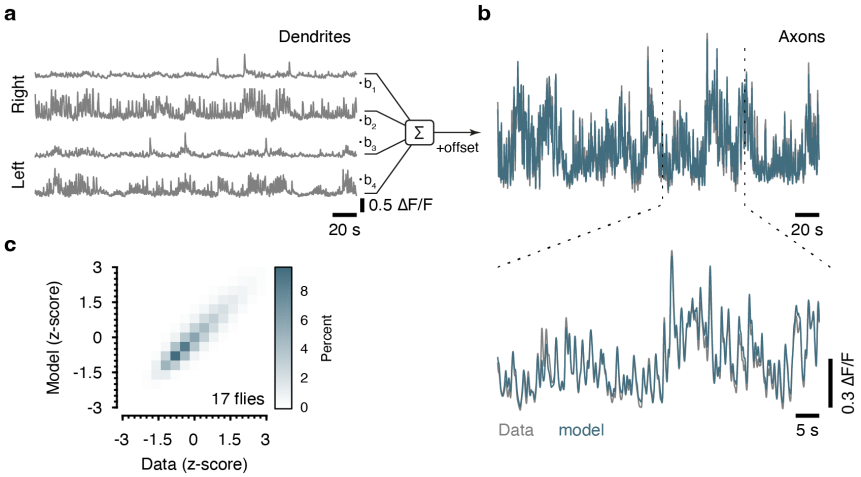

Supplementary Figure 1 | Simultaneous imaging of dFBN dendrites and axons.

a, **b**, Example GCaMP traces of dFBN dendrites (**a**) and axons (**b**). A linear model using the dendritic signals as predictor variables (blue, 5-fold cross-validation) accurately describes the axonal GCaMP trace (gray), shown at an expanded time scale below (**b**). **c**, Two-dimensional histogram of measured vs. predicted axonal GCaMP signals (5-fold cross-validation). Data in the histogram were z-score-normalized for display but not for fitting and are color-coded according to the key on the right. For imaging details see Supplementary Table 1.

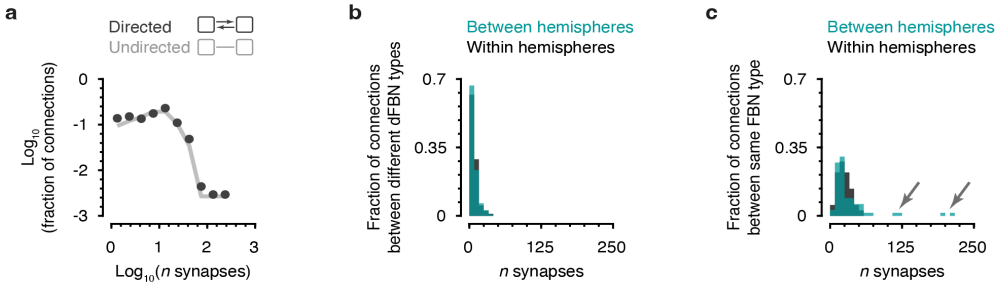

Supplementary Figure 2 | Connectomic support for a half-centre oscillator.

a, Histogram (log-log-scale) of the number of synapses per inter-dFBN-connection in the hemibrain v1.1 dataset. *n*=31 dFBNs projecting to layers 6 and 7. Conversion of directed (dark gray) to undirected edges (light gray) leaves the histogram unchanged, indicating a symmetric connectivity matrix. **b**, Histogram of inter- (green) and intra-hemispheric connections (black) between different dFBN types (e.g., FB6A to FB7K). **c**, Histogram of inter- (green) and intra-hemispheric connections (black) between the same dFBN types (e.g., FB6A to FB6A). The average number of synapses between the same dFBN types (29.96, **c**) is larger than the average number of synapses between different dFBN types (7.62, **b**) (P<0.0001, Mann-Whitney test). Four purely interhemispheric, reciprocally symmetric connections are formed by more than 100 synapses each: Left arrow, FB6A_L and FB6A_R (cell_1105955480 and cell_946308203); 112 synapses FB6A_L-to-FB6A_R and 124 synapses FB6A_R-to-FB6A_L. Right arrow, FB6E_L and FB6E_R (cell_422876942 and cell_5813049824); 211 synapses FB6E_L-to-FB6E_R and 195 synapses FB6E_R-to-FB6E_L. For statistical details see Supplementary Table 3.

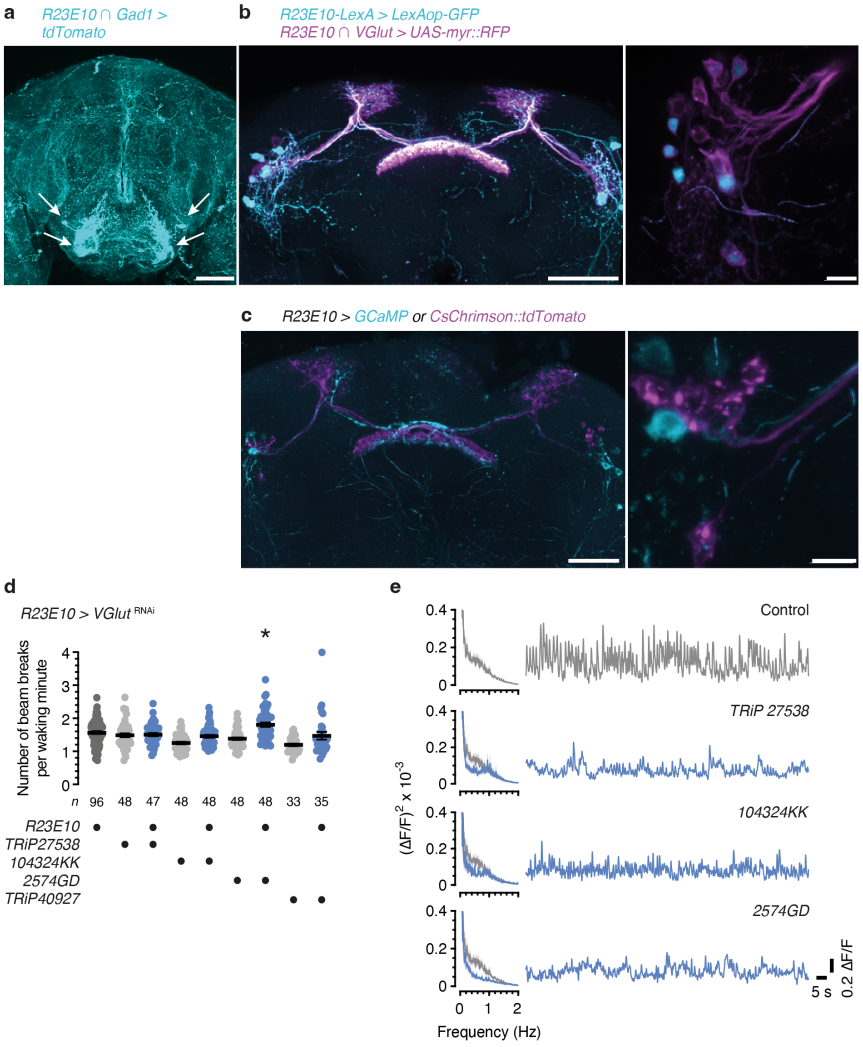

Supplementary Figure 3 | dFBNs promote sleep via glutamate.

a, Maximum-intensity projection of a fly brain expressing tdTomato under the control of *R23E10 ∩ Gad1-GAL4*. Arrows indicate two pairs of tdTomato-positive somata and their processes in the suboesophageal zone. Scale bar, 50 µm. **b**, Maximum-intensity projections of fly brains expressing GFP under the control of *R23E10-LexA* and myr::RFP under the control of *R23E10 ∩ VGlut-GAL4* (left, whole midbrain; right, dFBN somata). *R23E10 ∩ VGlut-GAL4* captures all dFBNs labelled by *R23E10-LexA*. Additional myr::RFP-positive dFBNs are included in the *R23E10-GAL4* pattern but missing from *R23E10-LexA*. Scale bars, 50 µm (left) and 10 µm (right). **c**, Maximum-intensity projections of fly brains expressing CsChrimson::tdTomato (magenta) or GCaMP (cyan) in a mutually-exclusive fashion after FLP-mediated recombination (left, whole midbrain; right, dFBN somata). Scale bars, 50 µm (left) and 10 µm (right). **d**, With the exception of flies carrying the *2574GD* construct ($P \leq 0.0033$, Holm-Šídák test after ANOVA), waking locomotor activity in flies expressing *R23E10-GAL4*-driven RNAi transgenes directed against VGlut is unchanged ($P \geq 0.3472$ relative to ≥1 parental control, Holm-Šídák test after ANOVA). **e**, Power spectra (left) and example dendritic GCaMP traces (right) of dFBNs expressing GCaMP without or with *R23E10-GAL4*-driven RNAi transgenes directed against VGlut. The asterisk indicates a significant difference ($P<0.05$) from both parental controls. Data are means ± s.e.m.; *n*, number of flies. For statistical details see Supplementary Table 3.

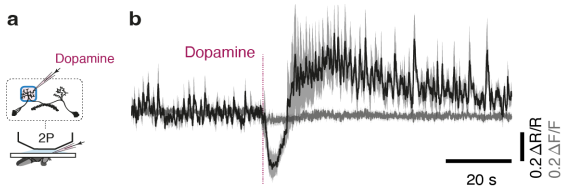

Supplementary Figure 4 | Dopamine inhibits dFBNs.

a, Imaging of dFBN dendrites during pressure ejection of 10 mM dopamine. **b**, Average GCaMP trace (black) normalized to mCD4::tdTomato fluorescence (ΔR/R) and aligned to a 640-ms dopamine pulse. Average ΔF/F of mCD4::tdTomato is shown for comparison (gray). *n*=8 ROIs in 4 flies. Data are means ± s.e.m. For imaging details see Supplementary Table 1.

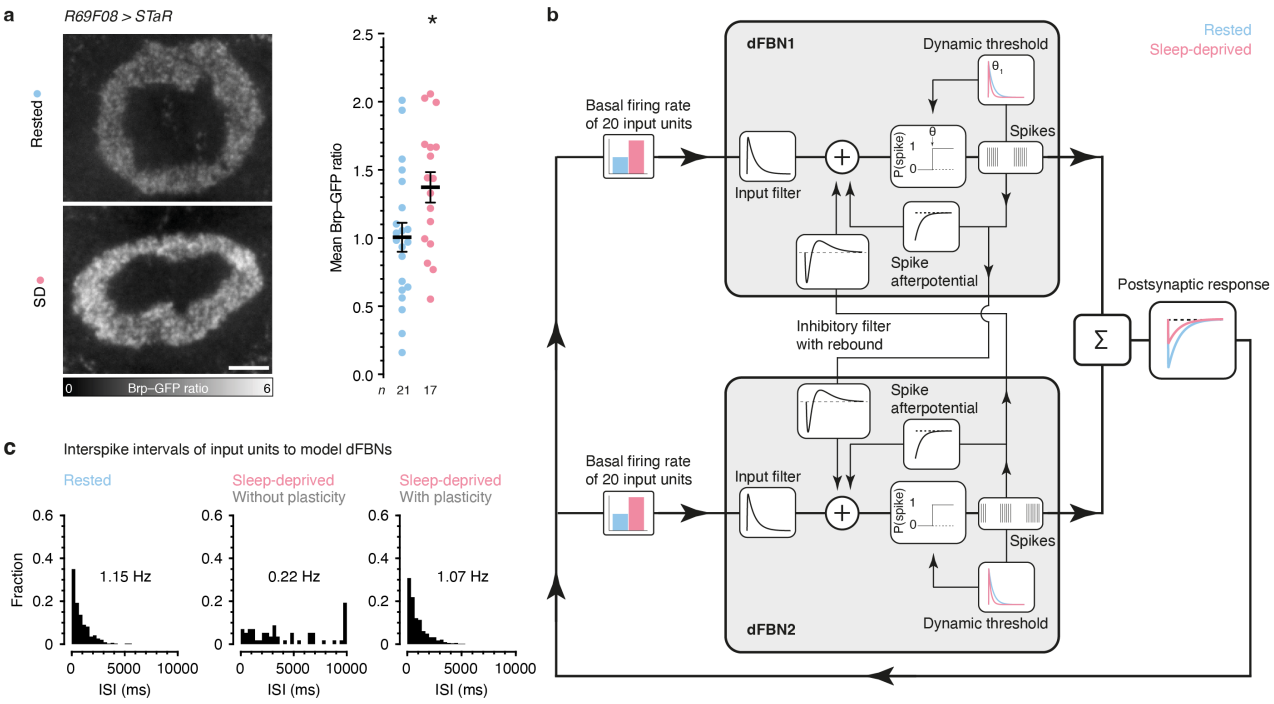

Supplementary Figure 5 | Efferent dFBN synapses depress after sleep deprivation.

a, Summed-intensity projections of V5-tagged endogenous BRP in R5 neuron axons coexpressing mCD8::GFP. Emission ratios are intensity-coded according to the key at the bottom and increase after sleep deprivation (SD) (P=0.0236, t test). Scale bar, 10 µm. **b**, Model architecture. dFBN1 and dFBN2 are each driven by 20 presynaptic units whose spike trains are inhomogeneous Poisson processes; the rates of these Poisson processes are subject to feedback inhibition by the summed spikes of both dFBNs. The membrane potential of each dFBN is a linear sum of resting potential, excitatory postsynaptic potentials due to Poisson units (input filter), inhibitory postsynaptic potentials and postinhibitory rebound due to the contralateral dFBN (inhibitory filter with rebound), and spike afterpotential. The membrane potential passes through a dynamic threshold to produce spikes. Color indicates sleep history-dependent variations in the basal firing rates of Poisson units, the dynamic threshold of dFBNs, and the postsynaptic response to transmission from dFBN synapses. **c**, Interspike interval (ISI) distributions of Poisson units at baseline and after sleep deprivation, in the absence and presence of plastic feedback connections from dFBNs. Data are means ± s.e.m.; asterisk, significant difference (P<0.05) in a planned pairwise comparison. For statistical details see Supplementary Table 3.

Supplementary Table 1. Imaging acquisition parameters.

Experiment and figures	N pixels (rows × columns)	Axial coordinates of focal planes (μm)†	Acquisition rate (Hz)¶	Sealed imaging window*	Additional details
Dendritic GCaMP imaging (Fig.1a, 2, 4, Supplementary Fig.1)	256 × 256	0, 10, 30, 40	14.56	Yes	ROI selection blind to sleep history and zeitgeber time. Data displayed in Fig.1a, 2, 4, and Supplementary Fig.1 are from the same dataset.
Cell body GCaMP imaging (Fig. 1b,c)	256 × 256	Four planes at variable distances of 0-30 μm	14.56	No	No between-group comparisons and thus no blinding during ROI selection. In some cases data were obtained from the left and right hemispheres of the same brain in separate imaging sessions. These were treated as independent experiments.
Simultaneous patch-clamp and GCaMP imaging (Fig.1d,e,f)	256 × 256	0	58.25	No	No between-group comparisons and thus no blinding during ROI selection.
Dendritic GCaMP imaging plus VGlut RNAi (Fig.3i, Supplementary Fig.3e)	256 × 256	0, 10, 20, 30	14.56	Yes	ROI selection blind to genotype.
iGluSnfR imaging during optogenetic stimulation of dFBNs (Fig.3d)	80 × 180	0	208.16	No	No between-group comparisons and thus no blinding during ROI selection. Stimulus-aligned traces are means of 40 repetitions per fly, applied every other s.
GCaMP imaging during optogenetic stimulation of a dFBN subset (Fig.3e)	256 × 256	Two planes at distances of 7-13 μm	29.13	No	ROI selection blind to dietary retinal and genotype. Stimulus-aligned traces are means of several simultaneously recorded cell bodies per fly, averaged over 10 repetitions (light applied every 20 s; 1-2, 1-3, and 1-5 cell bodies in flies expressing CsChrimson with retinal, CsChrimson without retinal, and no CsChrimson, respectively. In some cases data were obtained from the left and right hemispheres of the same brain. These were recorded in separate imaging sessions and averaged post hoc.
$GRAB_{DA2m}$ imaging during heat stimulation (Fig.5b)	256 × 256	0, 10, 20, 30	14.56	Yes	No between-group comparisons and thus no blinding during ROI selection.
Dendritic GCaMP imaging during heat stimulation (Fig. 5c,d,e)	256 × 256	0, 10, 20, 30	14.56	Yes	No between-group comparisons and thus no blinding during ROI selection.
$GRAB_{DA2m}$ imaging during optogenetic stimulation of dFBNs (Fig.5g)	256 × 256	0, 10, 20, 30	14.56	Yes	ROI selection blind to genotype.
iGluSnfR imaging during optogenetic stimulation of dFBNs after sleep deprivation (Fig.6b)	100 × 256	0, 10	68.32	Yes	ROI selection blind to sleep history. Stimulus-aligned traces are means from two simultaneously recorded axonal ROIs (different focal planes) and 5 repetitions (for each light intensity) per fly. The order in which stimuli with different intensities were applied was varied between flies to avoid adaptation. Flies were placed on retinal food after optical window implantation and kept on retinal food during sleep measurements.
Dendritic GCaMP imaging during focal dopamine application (Supplementary Fig.4)	256 × 256	Four planes at distances of 0-50 μm	14.56	No	No between-group comparisons and thus no blinding during ROI selection.

† In ascending order from ventral to dorsal.
¶ Volumetric rate in simultaneous recordings of more than one focal plane.
* If no sealed imaging window was used, dissections were done on the recording day and brains were superfused with extracellular solution (see Methods).

Supplementary Table 2. Statistical analyses of Figures 3–6.

Figure	Statistical test	Pairwise comparison	Test statistic	*P*
3e	One-way ANOVA Effect of optogenetic stimulation Holm-Šidák test Holm-Šidák test	 CsChrimson + retinal vs. GCaMP only CsChrimson + retinal vs. CsChrimson – retinal	 $F_{2,27}$=43.66 t_{27}=9.077 t_{27}=6.462	 <0.0001 <0.0001 <0.0001
3f	Wilcoxon test		W = -45	0.0039
3g, left	Mixed-effects model Time x retinal Time Retinal		 $F_{23,2869}$ = 2.887 $F_{15.65,1953}$ = 15.07 $F_{1,125}$ = 6.107	 <0.0001 <0.0001 0.0148
3g, right	Kruskal-Wallis ANOVA Effect of retinal and stimulation pattern Dunn's test Dunn's test Dunn's test	 + Retinal (bursts) vs. – Retinal (bursts) + Retinal (bursts) vs. + Retinal (tonic) – Retinal (bursts) vs. + Retinal (tonic)	 H_3 = 20.33 Z = 3.809 Z = 3.487 Z = 0.6498	 <0.0001 0.0004 0.0015 >0.9999
3h	One-way ANOVA Genotype Holm-Šidák test Holm-Šidák test Holm-Šidák test Holm-Šidák test Holm-Šidák test Holm-Šidák test Holm-Šidák test Holm-Šidák test	 *R23E10>VGlut*$^{RNAi\ TRiP\ \#27538}$ vs. *R23E10* *R23E10>VGlut*$^{RNAi\ TRiP\ \#27538}$ vs. *VGlut*$^{RNAi\ TRiP\ \#27538}$ *R23E10>VGlut*$^{RNAi\ 104324KK}$ vs. *R23E10* *R23E10>VGlut*$^{RNAi\ 104324KK}$ vs. *VGlut*$^{RNAi\ 104324KK}$ *R23E10>VGlut*$^{RNAi\ 2574GD}$ vs. *R23E10* *R23E10>VGlut*$^{RNAi\ 2574GD}$ vs. *VGlut*$^{RNAi\ 2574GD}$ *R23E10>VGlut*$^{RNAi\ TRiP\ \#40927}$ vs. *R23E10* *R23E10>VGlut*$^{RNAi\ TRiP\ \#40927}$ vs. *VGlut*$^{RNAi\ TRiP\ \#40927}$	 $F_{8,442}$ = 20.16 t_{442} = 7.497 t_{442} = 6.782 t_{442} = 7.488 t_{442} = 2.881 t_{442} = 8.919 t_{442} = 5.084 t_{442} = 4.090 t_{442} = 2.903	 <0.0001 <0.0001 <0.0001 <0.0001 0.0077 <0.0001 <0.0001 0.0002 0.0077
3i	One-way ANOVA Genotype Holm-Šidák test Holm-Šidák test Holm-Šidák test	 *R23E10* vs. *R23E10>VGlut*$^{RNAi\ TRiP\ \#27538}$ *R23E10* vs. *R23E10>VGlut*$^{RNAi\ 104324KK}$ *R23E10 vs. R23E10>VGlut*$^{RNAi\ 2574GD}$	 $F_{3,46}$ = 7.153 t_{46} = 2.702 t_{46} = 3.024 t_{46} = 4.252	 0.0005 0.0096 0.0081 0.0003
3j, left	Two-way repeated-measures ANOVA Time x genotype Time Genotype		 $F_{142,7952}$ = 15.47 $F_{1.451,162.5}$ = 262.5 $F_{2,112}$ = 8.458	 <0.0001 <0.0001 0.0004
3j, centre	Two-way repeated-measures ANOVA Time x genotype Time Genotype		 $F_{142,8520}$ = 7.611 $F_{1.364,163.7}$ = 178.4 $F_{2,120}$ = 3.092	 <0.0001 <0.0001 0.0004
3j, right	Kruskal-Wallis ANOVA Genotype Dunn's test Dunn's test Dunn's test Dunn's test	 *R23E10>VGlut*$^{RNAi\ TRiP\ \#27538}$ vs. *R23E10* *R23E10>VGlut*$^{RNAi\ TRiP\ \#27538}$ vs. *VGlut*$^{RNAi\ TRiP\ \#27538}$ *R23E10>VGlut*$^{RNAi\ 104324KK}$ vs. *R23E10* *R23E10>VGlut*$^{RNAi\ 104324KK}$ vs. *VGlut*$^{RNAi\ 104324KK}$	 H_5 = 56.92 Z = 5.855 Z = 2.982 Z = 3.188 Z = 3.937	 <0.0001 <0.0001 0.0115 0.0057 0.0003
4b	Mann-Whitney test		U = 24	0.0028
4d	Mixed-effects model Time x sleep history Time Sleep history Holm-Šidák test Holm-Šidák test Holm-Šidák test	 Morning (Rested vs. sleep-deprived) Evening (Rested vs. sleep-deprived) Following morning (Rested vs. sleep-deprived)	 $F_{2,37}$ = 4.197 $F_{1.671,30.92}$ = 3.904 $F_{1,42}$ = 1.087 $t_{22.67}$=2.786 $t_{35.28}$=0.8923 $t_{10.12}$=2.200	 0.0228 0.0375 0.3031 0.0314 0.3783 0.1015
5f	Two-way repeated-measures ANOVA Time x genotype Time Genotype Holm-Šidák test Holm-Šidák test Holm-Šidák test	 Pre (- *Chrimson* vs. + *Chrimson*) Light (- *Chrimson* vs. + *Chrimson*) Post (- *Chrimson* vs. + *Chrimson*)	 $F_{2,42}$ = 7.469 $F_{2,42}$ = 14.74 $F_{1,21}$ = 22.66 t_{63} = 1.404 t_{63} = 6.027 t_{63} = 2.153	 0.0017 <0.0001 0.0001 0.1652 <0.0001 0.0691
6a	Unpaired *t* test		t_{49} = 3.522	0.0009
6b	Two-way repeated-measures ANOVA Light intensity x sleep history		 $F_{4,84}$ = 6.120	 0.0002

	Light intensity Sleep history		$F_{1.189,24.96} = 338.3$ $F_{1,21} = 3.998$	<0.0001 0.0587

Supplementary Table 3. Statistical analyses of Supplementary Figures 2–4.

Figure (ED)	Statistical test	Pairwise comparison	Test statistic	*P*
2b-c	Mann-Whitney test		$U = 5285$	<0.0001
3d	One-way ANOVA Genotype		$F_{8,442} = 9.791$	<0.0001
	Holm-Šidák test	*R23E10>VGlut*$^{RNAi\ TRiP\ \#27538}$ vs. *R23E10*	$t_{442} = 0.8656$	0.6245
	Holm-Šidák test	*R23E10>VGlut*$^{RNAi\ TRiP\ \#27538}$ vs. *VGlut*$^{RNAi\ TRiP\ \#27538}$	$t_{442} = 0.2347$	0.8145
	Holm-Šidák test	*R23E10>VGlut*$^{RNAi\ 104324KK}$ vs. *R23E10*	$t_{442} = 1.643$	0.3472
	Holm-Šidák test	*R23E10>VGlut*$^{RNAi\ 104324KK}$ vs. *VGlut*$^{RNAi\ 104324KK}$	$t_{442} = 2.614$	0.0454
	Holm-Šidák test	*R23E10>VGlut*$^{RNAi\ 2574GD}$ vs. *R23E10*	$t_{442} = 3.519$	0.0033
	Holm-Šidák test	*R23E10>VGlut*$^{RNAi\ 2574GD}$ vs. *VGlut*$^{RNAi\ 2574GD}$	$t_{442} = 5.397$	<0.0001
	Holm-Šidák test	*R23E10>VGlut*$^{RNAi\ TRiP\ \#40927}$ vs. *R23E10*	$t_{442} = 1.241$	0.5170
	Holm-Šidák test	*R23E10>VGlut*$^{RNAi\ TRiP\ \#40927}$ vs. *VGlut*$^{RNAi\ TRiP\ \#40927}$	$t_{442} = 2.981$	0.0181
5a	Unpaired *t* test		$t_{36} = 2.364$	0.0236